Blockade of NOX2 and STIM1 signaling limits lipopolysaccharide-induced vascular inflammation

Rajesh Kumar Gandhirajan,[1,2] Shu Meng,[3] Harish C. Chandramoorthy,[1,2] Karthik Mallilankaraman,[1,2] Salvatore Mancarella,[1] Hui Gao,[4] Roshanak Razmpour,[5] Xiao-Feng Yang,[3] Steven R. Houser,[4] Ju Chen,[6] Walter J. Koch,[2,3] Hong Wang,[3] Jonathan Soboloff,[1] Donald L. Gill,[1] and Muniswamy Madesh[1,2]

[1]Department of Biochemistry, [2]Center for Translational Medicine, [3]Department of Pharmacology, [4]Department of Physiology, Cardiovascular Research Center, and [5]Department of Anatomy and Cell Biology, Temple University, Philadelphia, Pennsylvania, USA. [6]Department of Medicine, UCSD, La Jolla, California, USA.

During sepsis, acute lung injury (ALI) results from activation of innate immune cells and endothelial cells by endotoxins, leading to systemic inflammation through proinflammatory cytokine overproduction, oxidative stress, and intracellular Ca^{2+} overload. Despite considerable investigation, the underlying molecular mechanism(s) leading to LPS-induced ALI remain elusive. To determine whether stromal interaction molecule 1–dependent (STIM1-dependent) signaling drives endothelial dysfunction in response to LPS, we investigated oxidative and STIM1 signaling of EC-specific *Stim1*-knockout mice. Here we report that LPS-mediated Ca^{2+} oscillations are ablated in ECs deficient in *Nox2*, *Stim1*, and type II inositol triphosphate receptor (*Itpr2*). LPS-induced nuclear factor of activated T cells (NFAT) nuclear accumulation was abrogated by either antioxidant supplementation or Ca^{2+} chelation. Moreover, ECs lacking either *Nox2* or *Stim1* failed to trigger store-operated Ca^{2+} entry (SOCe) and NFAT nuclear accumulation. LPS-induced vascular permeability changes were reduced in EC-specific *Stim1*$^{-/-}$ mice, despite elevation of systemic cytokine levels. Additionally, inhibition of STIM1 signaling prevented receptor-interacting protein 3–dependent (RIP3-dependent) EC death. Remarkably, BTP2, a small-molecule calcium release–activated calcium (CRAC) channel blocker administered after insult, halted LPS-induced vascular leakage and pulmonary edema. These results indicate that ROS-driven Ca^{2+} signaling promotes vascular barrier dysfunction and that the SOCe machinery may provide crucial therapeutic targets to limit sepsis-induced ALI.

Introduction

The systemic inflammatory response in sepsis has devastating consequences resulting in high morbidity and mortality (1). It represents a major burden on the health care system, with more than 400,000 cases/year in the United States alone (1–4). Over the past decade, mortality from sepsis alone has remained greater than 25%, despite effective antimicrobial therapy. This highlights lack of understanding of the pathways operative in sepsis and the necessity for improved therapies. Impairment of pulmonary vascular integrity is a key feature in multiple pathological conditions, including acute lung injury (ALI), sepsis, lung inflammation, and ventilator-induced lung injury, each of which result in pulmonary edema (1, 5–7). Sepsis is a complex, serious medical condition consequent to an overwhelming immune response to infection. The systemic inflammatory response in sepsis can lead to rapid organ failure and death (1, 5). Bacterial endotoxin (LPS) ranks highest among risk factors contributing to ALI in sepsis (8). Endotoxins are known to activate innate immune responses, resulting in the production of a vast spectrum of inflammatory cytokines (1, 9). These proinflammatory cytokines are known to trigger vascular endothelial activation (5). The integrity of vascular endothelium is essential for controlling the flux of proteins, fluid, and immune cells across vessels into tissues. Systemic accumulation of LPS triggers leukocyte infiltration within the vascular wall and promotes vascular permeability (10). Therefore, maintenance of vascular integrity is crucial for vascular and tissue homeostasis. Although the LPS-induced signaling cascade has been widely studied in innate immune cells (11), the mechanisms mediating EC responses to LPS remain largely unknown.

Oxidative signaling and Ca^{2+} homeostasis are tightly linked cellular processes mediating control over signal transduction, metabolism, transcriptional regulation, cell proliferation, and cell death (12, 13). Oxidants are implicated in modulating intracellular Ca^{2+} release channels and Ca^{2+} entry channels in the plasma membrane (14–16). STIM-induced Ca^{2+} entry through Orai channels is now established as an essential Ca^{2+} entry mechanism in non-excitable cell types (17–22). STIM proteins are Ca^{2+} store sensors and mediate the induction of cellular responses to a number of stress conditions, including elevated ROS, temperature changes, and hypoxia (14, 19, 23, 24). Although oxidants and Ca^{2+} are essential regulators of vascular signaling in pathophysiological settings including innate inflammation (5), precisely how ECs respond to LPS remained unclear. Studies by us and others have demonstrated that ROS can modulate cytosolic Ca^{2+} signals generated through inositol 1,4,5-trisphosphate receptor ($InsP_3R$) Ca^{2+} release channels in ECs (15). More recently, we revealed that ROS can induce STIM-mediated Ca^{2+} entry via Orai channels by activating STIM proteins through *S*-glutathionylation of an evolutionarily conserved N-terminal cysteine residue in the STIM1 protein (14). Although ROS overproduction

Authorship note: Shu Meng and Harish C. Chandramoorthy contributed equally to this work.

Conflict of interest: The authors have declared that no conflict of interest exists.

Citation for this article: *J Clin Invest.* 2013;123(2):887–902. doi:10.1172/JCI65647.

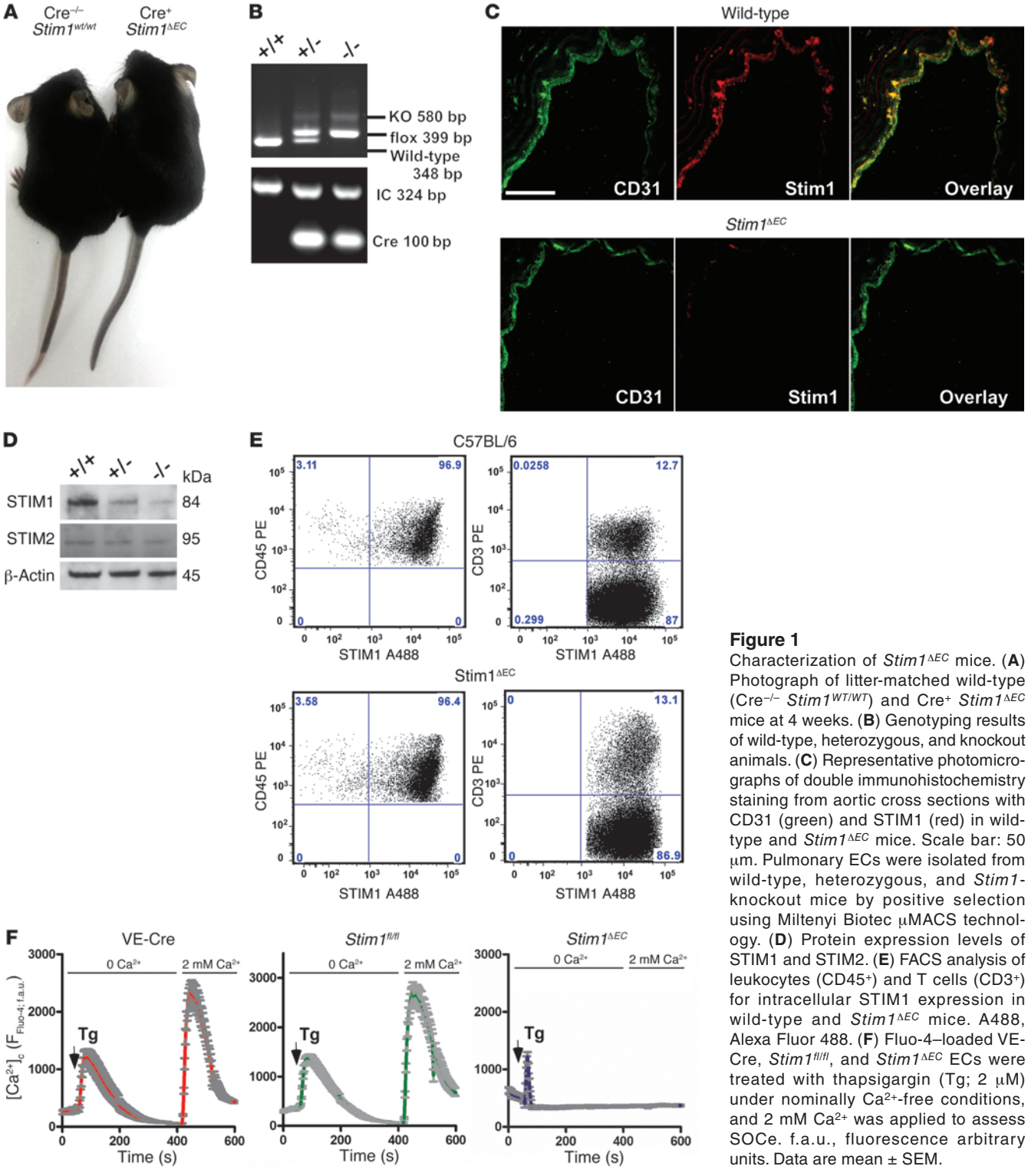

Figure 1
Characterization of *Stim1*$^{\Delta EC}$ mice. (**A**) Photograph of litter-matched wild-type (Cre$^{-/-}$ *Stim1*$^{WT/WT}$) and Cre^{+} *Stim1*$^{\Delta EC}$ mice at 4 weeks. (**B**) Genotyping results of wild-type, heterozygous, and knockout animals. (**C**) Representative photomicrographs of double immunohistochemistry staining from aortic cross sections with CD31 (green) and STIM1 (red) in wild-type and *Stim1*$^{\Delta EC}$ mice. Scale bar: 50 μm. Pulmonary ECs were isolated from wild-type, heterozygous, and *Stim1*-knockout mice by positive selection using Miltenyi Biotec μMACS technology. (**D**) Protein expression levels of STIM1 and STIM2. (**E**) FACS analysis of leukocytes (CD45^{+}) and T cells (CD3^{+}) for intracellular STIM1 expression in wild-type and *Stim1*$^{\Delta EC}$ mice. A488, Alexa Fluor 488. (**F**) Fluo-4–loaded VE-Cre, *Stim1*$^{fl/fl}$, and *Stim1*$^{\Delta EC}$ ECs were treated with thapsigargin (Tg; 2 μM) under nominally Ca^{2+}-free conditions, and 2 mM Ca^{2+} was applied to assess SOCe. f.a.u., fluorescence arbitrary units. Data are mean ± SEM.

is an established event upon LPS challenge, it remains unclear whether ROS/STIM1 signaling participates in TLR4-dependent EC activation, vascular permeability, and lung injury.

In most cells, the coordination of Ca^{2+} release and Ca^{2+} entry mechanisms gives rise to sustained Ca^{2+} oscillations essential for controlling cellular responses, including gene expression and cell fate (25). These responses are mediated by transcription factors, notably NF-κB (5) and NFAT (26). NFATs are members of a multi-gene Rel family of transcription factors. Nuclear localization of NFAT is primarily driven by Ca^{2+} oscillations mediated by a combination of $InsP_3Rs$ and STIM/Orai channels, resulting in control of Ca^{2+}-dependent transcription

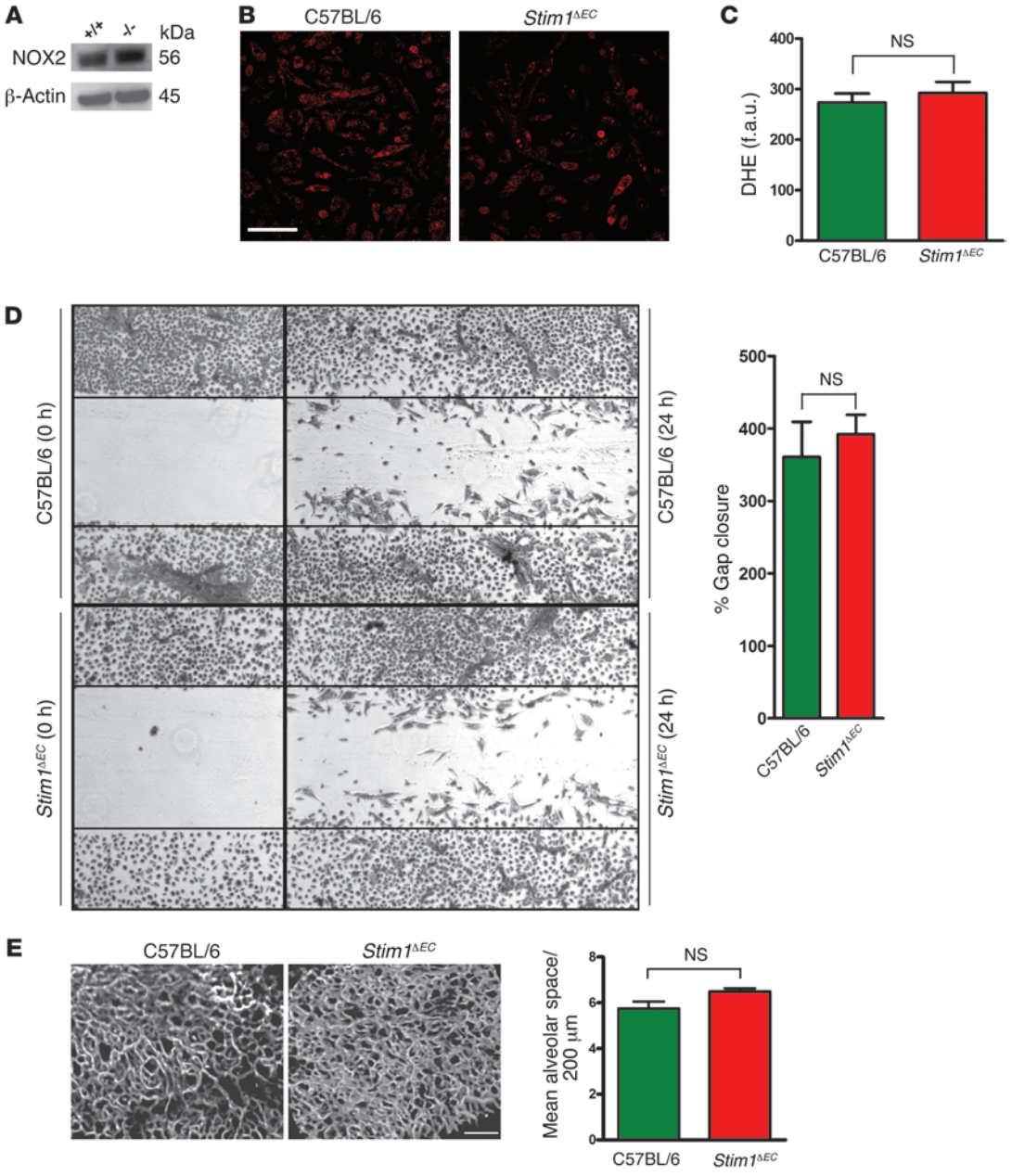

Figure 2

Stim1$^{\Delta EC}$ mice have normal pulmonary vasculature and endothelial migration. (**A**) NOX2 protein levels in ECs. (**B**) Representative images and (**C**) quantification of DHE fluorescence in ECs derived from wild-type and *Stim1*$^{\Delta EC}$ mice. Scale bar: 20 μm. (**D**) Representative images and quantification of gap closure in ECs derived from wild-type and *Stim1*$^{\Delta EC}$ mice at 24 hours. (**E**) Assessment of pulmonary vascular distribution by 2-photon imaging in 5-week-old litter-matched wild-type and *Stim1*$^{\Delta EC}$ mice after FITC-dextran administration. Bar graph shows quantification of mean alveolar space from **E**. Scale bar: 100 μm. Data are mean ± SEM.

in many cell types (19, 26). Although the NFAT pathway is responsible for cytokine production in T cell activation, its role in EC proinflammatory molecule expression and vascular inflammation has not previously been established. Therefore, targeting ROS/STIM1 signaling pathways offers an alternate strategy for the development of new therapies against sepsis-related ALI. In this study, we reveal a crucial role for NOX2-dependent STIM1 activation in the control of the cytosolic oscillations that drive EC activation. We demonstrate the interdependence of ROS and Ca^{2+} in eliciting proinflammatory signaling in ECs. Further, we show that LPS-mediated ALI is alleviated in EC-specific *Stim1*-knockout (*Stim1*$^{\Delta EC}$) mice. We further show that post-administration of the Ca^{2+} entry blocker N-(4-[3,5-bis(trifluoromethyl)-1H-pyrazol-1-yl]phenyl)-4-methyl-1,2,3-thiadiazole-5-carboxamide (BTP2) significantly alleviates pulmonary vascular inflammation and lung injury. Hence, we demonstrate the translational potential for a previously unstudied mechanism of EC activation.

Table 1
Breeding ratio and body weight of WT and *Stim1*$^{\Delta EC}$ mice

Sex	Breeding ratio	Fertility (%)	Genotype	Body weight (g)[A]
Male *Stim1*$^{\Delta EC}$	15/15	100	WT	28.06 ± 1.29
Female *Stim1*$^{\Delta EC}$	2/6	33	*Stim1*$^{\Delta EC}$	25.63 ± 1.68

Breeding ratio values indicate male *Stim1*$^{\Delta EC}$ mice bred with female heterozygotes or female *Stim1*$^{\Delta EC}$ mice bred with male heterozygotes. Mean ± SEM values of WT and *Stim1*$^{\Delta EC}$ mice body weight are shown. [A]$P < 0.3$ compared with WT mice.

Results

EC-specific Stim1-knockout mice preserve normal pulmonary vasculature and endothelial migration. To investigate the in vivo role of STIM1-dependent Ca^{2+} entry pathways in ECs, we generated EC-specific *Stim1* conditional knockout mice (*Stim1*$^{\Delta EC}$) by flox-Cre recombination as described in Methods (Figure 1, A and B). The endothelial specificity and efficacy of the STIM1 ablation were confirmed by immunohistochemistry of aortic endothelium (Figure 1C) and immunoblotting of enriched pulmonary ECs (Figure 1D). To further verify whether STIM1 expression is normal in immune cells, we stained leukocytes from spleen of wild-type and *Stim1*$^{\Delta EC}$ mice for phenotypic surface markers and intracellular STIM1 expression. STIM1 protein expression was normal in $CD45^+$ and $CD3^+$ lymphocytes (Figure 1E). For functional studies, we measured SOCe in ECs derived from Stim1$^{\Delta EC}$, VE-Cre, or Stim1$^{fl/fl}$ mice and observed loss of SOCe in Stim1$^{\Delta EC}$ mice but not in controls (Figure 1F). Notably, ER Ca^{2+} levels were lower in *Stim1*$^{\Delta EC}$ when compared with VE-Cre or *Stim1*$^{fl/fl}$ mice ECs, as measured by store depletion using thapsigargin (Figure 1F). Our results are consistent with lower ER Ca^{2+} levels in ECs derived from hyperglycemic mice due to the downregulation of STIM1 and SERCA3 expression (27). To examine whether loss of STIM1 alters NOX2-mediated ROS production, we measured NOX2 protein expression and superoxide production in *Stim1*$^{\Delta EC}$ ECs. NOX2 protein expression and superoxide production remained unaltered in *Stim1*$^{\Delta EC}$ ECs (Figure 2, A–C). Although *Stim1*$^{\Delta EC}$ mice maintained relatively normal body weight without any gross phenotypic abnormalities (Table 1), *Stim1*$^{\Delta EC}$ female mice displayed a reproductive defect when bred with male heterozygote mice (Table 1). Further characterization of *Stim1*$^{\Delta EC}$ mice revealed that endothelial migration (Figure 2D) and pulmonary vascular distribution (Figure 2E) were normal when compared with those in wild-type mice. Together, these data show that ECs lacking STIM1 retain normal angiogenic potential and vascular integrity.

LPS-mediated lung inflammation is attenuated in EC-specific Stim1-knockout mice. We previously demonstrated that oxidants promote $InsP_3R$- and STIM1-dependent Ca^{2+} signaling and cell injury in LPS-challenged cells (14, 15). These findings led us to speculate that blockade of the Ca^{2+} permeation pathway could prevent LPS-induced lung inflammation and vascular injury. In *Stim1*$^{\Delta EC}$ mouse lungs, the relative alveolar space distribution was similar to that in controls (Figure 2E and Figure 3A). LPS-induced lung injury studies showed that leukocyte infiltration was significantly reduced in *Stim1*$^{\Delta EC}$ mice (Figure 3, A and B), despite systemic elevation of proinflammatory cytokines (Figure 3C). Additionally, we measured proinflammatory cytokine levels in BAL fluid obtained from control and *Stim1*$^{\Delta EC}$ mice. Interestingly, BAL fluid cytokine levels were elevated in control but remained unaltered in *Stim1*$^{\Delta EC}$ mice (Figure 3D). These data suggest that the lack of STIM1 in endothelium resulted in reduced endothelial activation despite systemic proinflammatory cytokine elevation.

To further explore whether endothelial *Stim1* deletion limits LPS-induced pulmonary vascular permeability, we administered LPS in VE-Cre, *Stim1*$^{fl/fl}$, and *Stim1*$^{\Delta EC}$ mice. Immunolabeling for ICAM-1 protein expression in *Stim1*$^{\Delta EC}$ lung sections revealed low ICAM-1 expression levels when compared with VE-Cre or *Stim1*$^{fl/fl}$ controls (Figure 4 A and B). We next assessed the BAL fluid accumulation and lung wet/dry ratio, which are indications of lung edema. Examination of BAL protein and lung wet/dry ratio showed that *Stim1*$^{\Delta EC}$ mice were protected from LPS-induced inflammatory changes in the lung (Figure 4, C and D). Although increase in systemic proinflammatory cytokine levels was observed in *Stim1*$^{\Delta EC}$ mice, the absence of leukocyte infiltration, BAL fluid, and change in lung weight, revealed that STIM1 was required for LPS-induced EC activation and lung inflammation. We then assessed the vascular integrity in *Stim1*$^{\Delta EC}$ mice challenged with LPS. Interestingly, the vasculature in LPS-treated *Stim1*$^{\Delta EC}$ mice, comparable to that in their untreated counterparts, was intact, whereas the vasculature was leaky in LPS-treated control (VE-Cre and *Stim1*$^{fl/fl}$) mice (Figure 4, E and F). These findings suggest that EC STIM1 is necessary for pathological changes during inflammation.

STIM1-dependent Ca^{2+} signaling contributes to endothelial NFAT activation. We previously showed that inhibition of STIM1/Orai1-mediated Ca^{2+} entry prevented oxidative stress–induced cell death (14, 28). Since endothelial STIM1 deficiency prevents LPS-induced vascular permeability, we examined pulmonary vascular Ca^{2+} levels in situ. Lungs were isolated from vehicle- and LPS-treated wild-type mice after 20 hours. Lung slices were generated and loaded with the Ca^{2+} indicator Fluo-4 and the endothelial marker AcLDL (Figure 5A). Viable lung slices were subjected to multiphoton confocal imaging, and Ca^{2+} levels were measured. As expected, basal cytoplasmic Ca^{2+} levels were elevated in LPS-treated when compared with untreated wild-type mouse lung slices (Figure 5, A and B). To determine whether STIM1-dependent Ca^{2+} signaling was involved in LPS-induced endothelial Ca^{2+} elevation, we measured dynamic Ca^{2+} changes in primary ECs isolated from wild-type and *Stim1*$^{\Delta EC}$ mice. Interestingly, LPS treatment triggered sustained Ca^{2+} oscillations in wild-type but not in *Stim1*$^{\Delta EC}$ ECs (Figure 5, C and D). Since Ca^{2+} oscillations are essential for NFAT nuclear translocation and transcriptional activation (29), we next assessed NFATC3-GFP translocation in wild-type and *Stim1*$^{\Delta EC}$ ECs after LPS challenge. Consistent with our sustained Ca^{2+} oscillation data (Figure 5C), *Stim1*$^{\Delta EC}$ ECs showed a significant reduction in nuclear accumulation of NFATC3-GFP compared with wild-type ECs (Figure 5, E and F). Further, we measured NFAT activity in wild-type and *Stim1* shRNA knockdown (KD) ECs (Supplemental Figure 4A; supplemental material available online with this article; doi:10.1172/JCI65647DS1) after stimulation with LPS. LPS-induced NFAT luciferase activity was markedly reduced in *Stim1* KD ECs when compared with wild-type ECs (Figure 5G). Similarly, the Ca^{2+} blocker BTP2 also near completely inhibited NFAT translocation upon LPS exposure (Supplemental Figure 1, A and B). Interestingly, NFAT-driven cytokine expression levels were downregulated in ECs derived from *Stim1*$^{\Delta EC}$ mice (Figure 5H). Thus, these data suggest that STIM1-mediated Ca^{2+} entry is necessary for LPS-induced NFAT activation and inflammatory cytokine production.

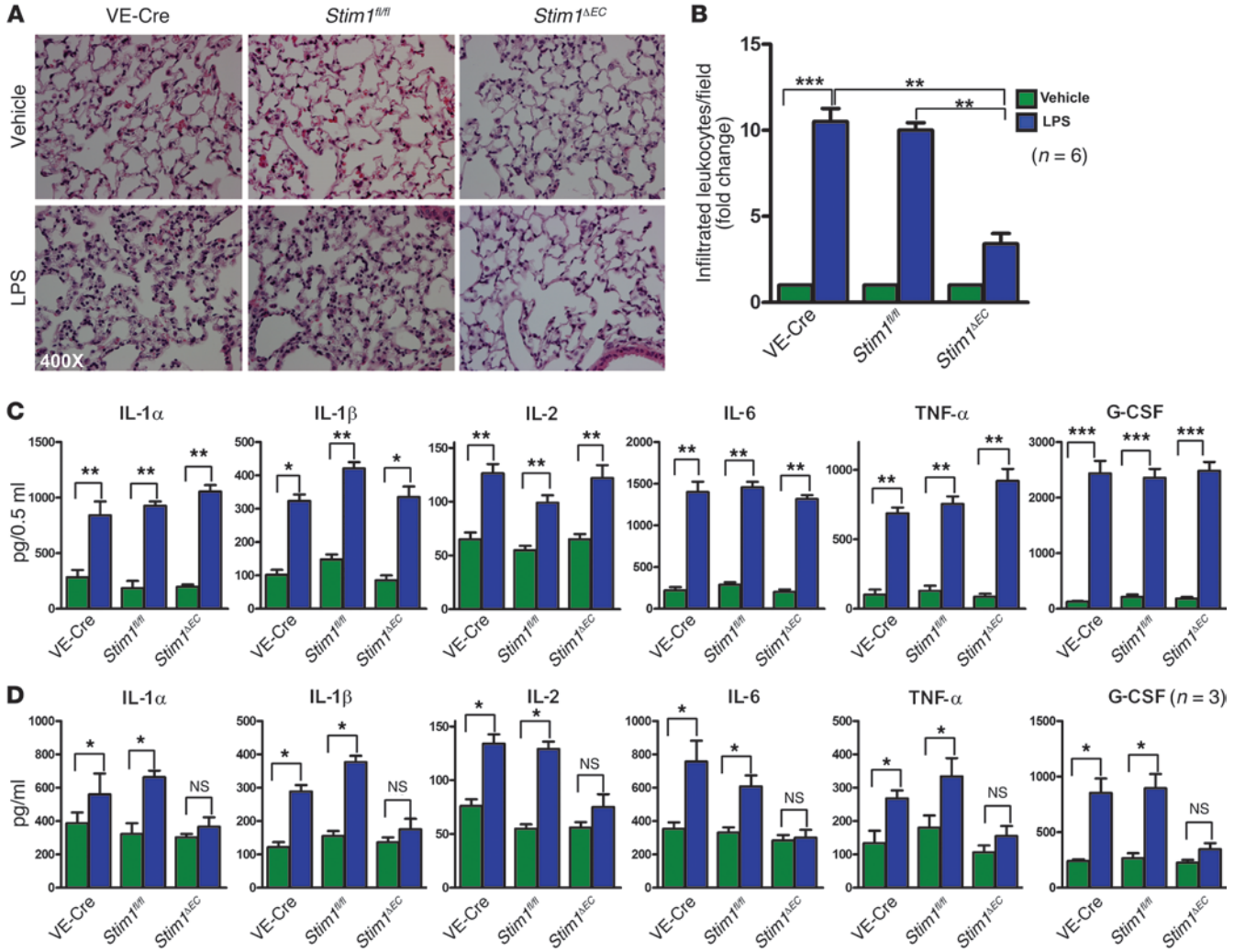

Figure 3

Genetic ablation of *Stim1* in endothelium limits LPS-induced leukocyte infiltration and BAL inflammatory cytokines. VE-Cre, *Stim1*$^{fl/fl}$, and *Stim1*$^{\Delta EC}$ mice were challenged with LPS (1 mg/kg; i.p.). Saline was used as a vehicle control. (**A**) Representative photomicrographs of H&E-stained lung sections. (**B**) Quantification of alveolar leukocyte infiltration. (**C**) IL-1α, IL-1β, IL-2, IL-6, TNF-α, and G-CSF were measured in sera from mice. (**D**) IL-1α, IL-1β, IL-2, IL-6, TNF-α, and G-CSF were measured in BAL fluid from VE-Cre, *Stim1*$^{fl/fl}$, and *Stim1*$^{\Delta EC}$ mice. Data are mean ± SEM. $^{*}P < 0.05$, $^{**}P < 0.01$, $^{***}P < 0.001$.

gp91^{phox}*, InsP*$_3$*RII, and STIM1 are necessary for LPS-induced endothelial* Ca^{2+} *oscillations.* LPS is a potent inducer of ROS through TLR4 (30, 31). We have previously shown that in lymphocytes, LPS-induced oxidative stress alters Ca^{2+} signaling (14). It is plausible that similar events occur in pulmonary vascular endothelium following LPS challenge and trigger increased vascular permeability. To test this hypothesis, we treated wild-type murine pulmonary vascular ECs (MPMVECs) with LPS (1 μg/ml). MPMVECs stably expressing the hydrogen peroxide (H_2O_2) sensor HyPer-Cyto exhibited a significant elevation of H_2O_2 levels after LPS challenge (Supplemental Figure 2, A and B). As expected, LPS stimulation triggered asynchronous Ca^{2+} oscillations in MPMVECs when compared with the untreated control cells (Supplemental Figure 2, C, D, H, I, and Supplemental Videos 1 and 2). Interestingly, we found that pretreatment with the NOX2 inhibitor diphenyleneiodonium (DPI) abrogated Ca^{2+} oscillations (Supplemental Figure 2, E and H). We examined whether LPS promotes Ca^{2+} oscillations in other cell types, including fibroblasts and lung epithelial and macrophage cell lines. Interestingly, LPS was not able to stimulate Ca^{2+} oscillations in fibroblasts and lung alveolar epithelial cell lines (Supplemental Figure 2, J and K). However, as expected, the J774.A1 macrophage cell line elicited basal Ca^{2+} oscillations due to constitutive phagocytic NOX2 activity (Supplemental Figure 2J). Additionally, LPS-induced Ca^{2+} oscillations were enhanced in J774.A1 macrophages, which are DPI sensitive (Supplemental Figure 2, K and L). We next examined whether extracellular Ca^{2+} entry is required for LPS-induced Ca^{2+} oscillations. Either chelating extracellular Ca^{2+} using EGTA or blocking Ca^{2+} entry using BTP2 prevented LPS-induced Ca^{2+} oscillations (Supplemental Figure 2, F–H). These data collectively suggest that endogenous ROS production is essential but requires Ca^{2+} entry to trigger EC Ca^{2+} oscillations.

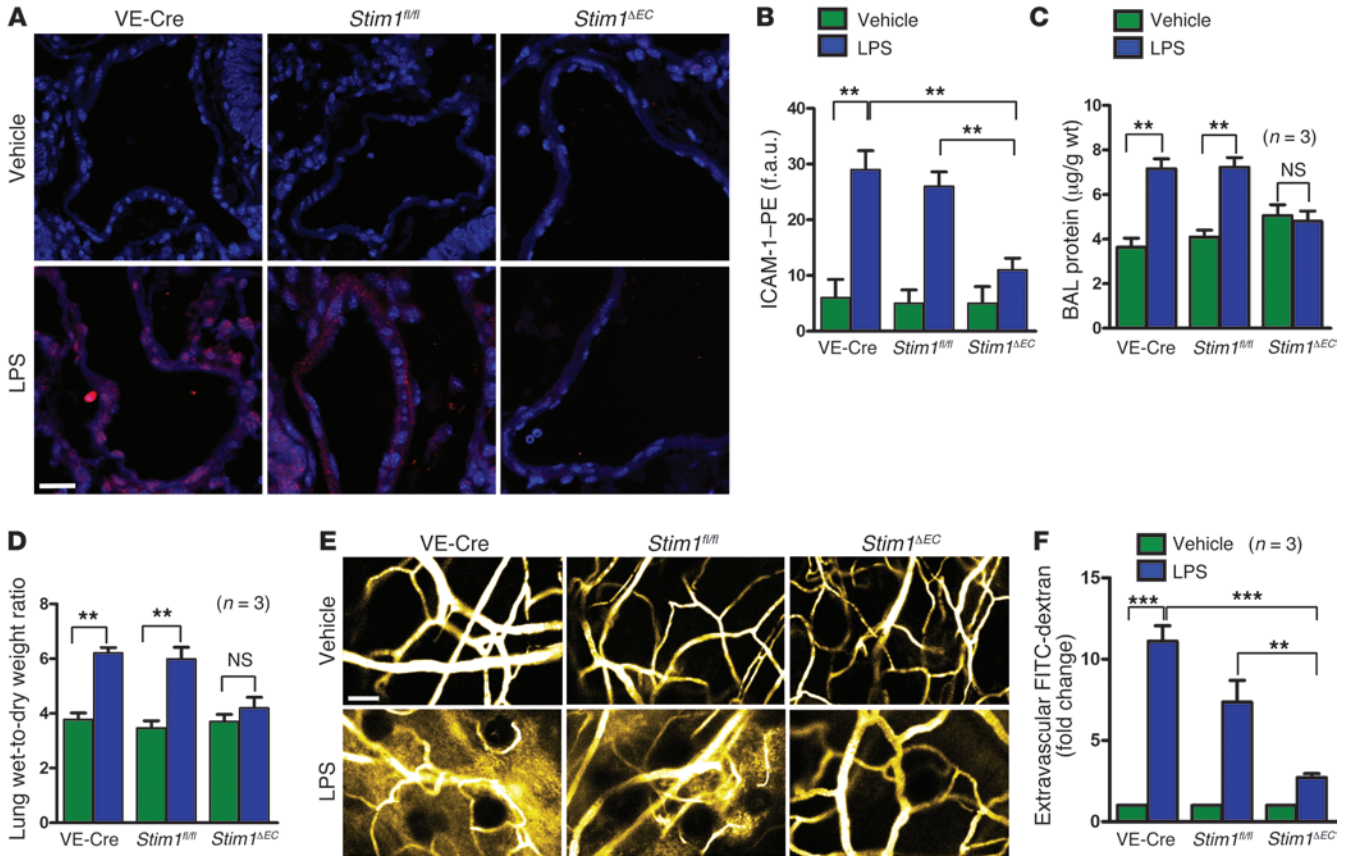

Figure 4

Stim1 deletion in endothelium attenuates LPS-induced pulmonary vascular dysfunction. (**A**) Representative immunohistochemistry images of ICAM-1 using PE in lung sections from treated mice. Scale bar: 20 μm. (**B**) Quantification of ICAM-1 expression based on fluorescence intensity. (**C**) BAL protein content and (**D**) lung weight changes are a functional measure of EC activation associated with increased vascular permeability. (**E**) A 0.1- to 0.15-ml bolus of FITC-dextran (70 kDa, 5%w/v) was injected into the animals via facial vein. Anesthetized animals were placed under an intravital 2-photon imaging system, and images were acquired. Vascular permeability was assessed based on fluorescence intensity in the extravascular space. Scale bar: 100 μm. (**F**) Quantification of extravascular FITC-dextran fluorescence intensity. Data are mean ± SEM. $^{**}P < 0.01$, $^{***}P < 0.001$.

We further verified the observed pharmacological effects in ECs lacking the NOX2 subunit gp^{91phox}. Similarly, $gp91^{phox-/-}$ ECs failed to elicit LPS-induced Ca^{2+} oscillations (Supplemental Figure 3, C and F, and Supplemental Videos 3 and 4). However, treatment of ECs derived from wild-type mice with LPS triggered Ca^{2+} oscillations (Supplemental Figure 3, A, B, and F). Sustained Ca^{2+} oscillations operate through the coordinated activation of both store-derived Ca^{2+} release and store-operated Ca^{2+} entry channels (25, 32). In non-excitable cells such as ECs, $InsP_3$Rs are the major ER Ca^{2+} release channels activated by $InsP_3$ produced when phospholipase C–coupled (PLC-coupled) receptors are activated (33). We have previously shown that ROS evokes intracellular Ca^{2+} mobilization in ECs (15, 34). To identify the intracellular Ca^{2+} release component in LPS-induced Ca^{2+} oscillations, we treated wild-type MPMVECs with LPS in the presence of the PLC inhibitor U73122 or the potent $InsP_3$R inhibitor xestospongin B (XesB), and the results revealed suppression of Ca^{2+} oscillations mediated by both LPS and the glutathione-depleting agent DL-buthionine sulfoximine (BSO) (our unpublished observations). Interestingly, similar to $Stim1^{\Delta EC}$ ECs (Supplemental Figure 3, E and F, and Supplemental Videos 5 and 6), ECs lacking only $InsP_3$R II also did not show any Ca^{2+} oscillations after LPS treatment (Supplemental Figure 3, D and F). These results suggest that LPS-induced NOX2-mediated Ca^{2+} oscillations in ECs require $InsP_3$RII-mediated Ca^{2+} release in addition to STIM1-dependent Ca^{2+} entry.

NOX2-derived ROS activates STIM1-dependent Ca^{2+} entry in LPS-stimulated ECs. Recent investigations revealed an essential role for STIM1-dependent Ca^{2+} entry in the induction of NFAT nuclear localization in activated lymphocytes and mast cells (26, 35). Nevertheless, the role of LPS-induced ROS-mediated Ca^{2+} elevation in transcriptional regulation has not previously been examined. Therefore, we redesigned our protocol to assess SOCe in LPS-challenged cells by briefly removing extracellular Ca^{2+} and then adding it back. Wild-type ECs exhibited greatly elevated Ca^{2+} entry in LPS-treated cells (Figure 6A). As expected, *Stim1* KD abrogated SOCe entry in ECs (Figure 6C). Intriguingly, LPS-induced Ca^{2+} entry was also abolished in ECs derived from $gp91^{phox-/-}$ mice, indicating that NOX2 is required for LPS-induced SOCe (Figure 6B). Further, loss of either NOX2 or STIM1 prevented LPS-induced nuclear localization of NFAT (Figure 6D and Supplemental Figure 4B), revealing the critical link between SOCe and NFAT activation.

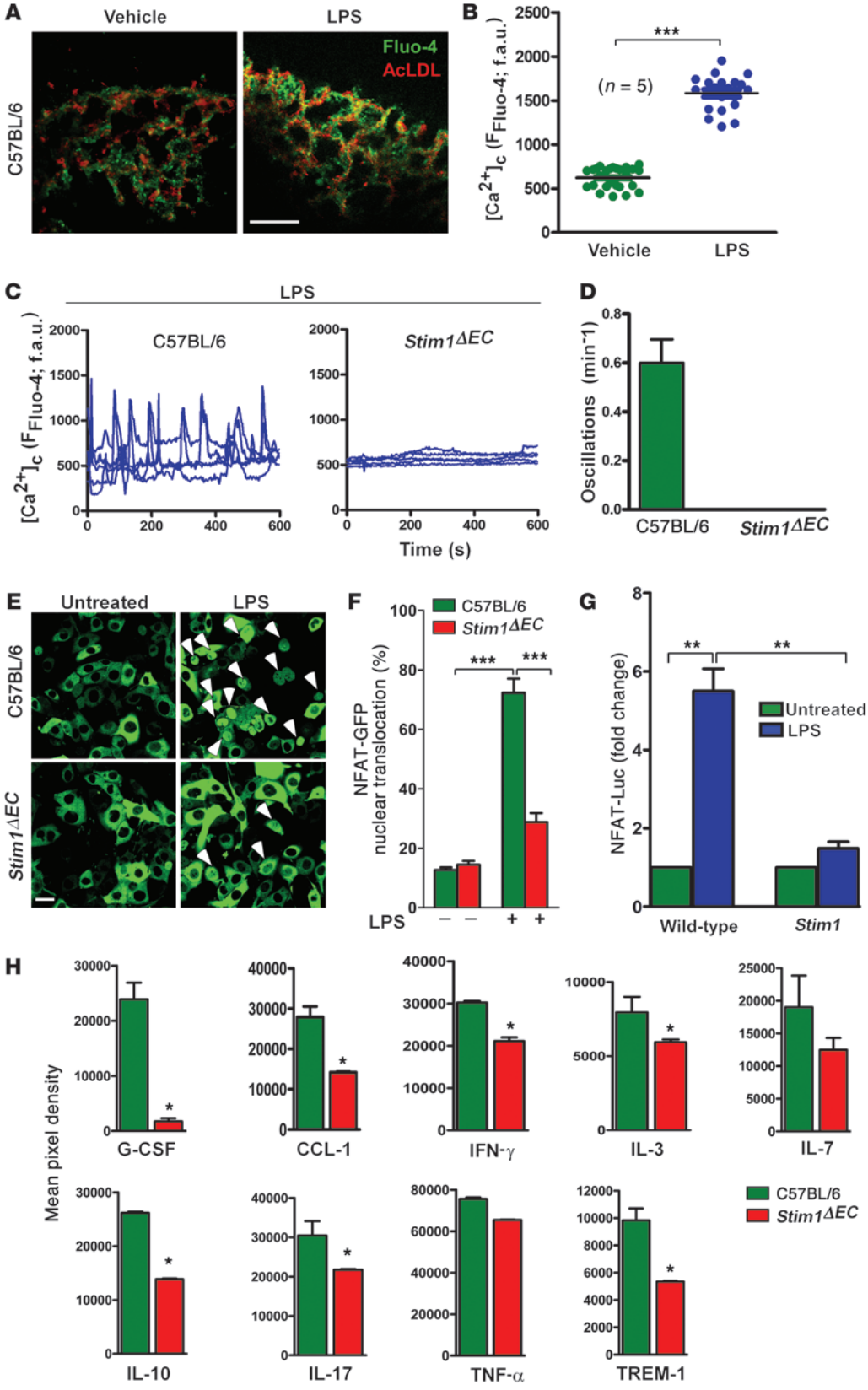

Figure 5

STIM1-mediated NFAT activity is necessary for LPS-induced proinflammatory gene expression in ECs. (**A**) Ex vivo imaging of pulmonary vascular Ca^{2+} levels in freshly prepared lung slices from wild-type mice challenged with LPS (1 mg/kg) for 20 hours. AcLDL was used as an endothelial marker. Scale bar: 50 μm. (**B**) Quantification of Fluo-4 fluorescence was measured from multiple regions of the lung slices. ECs from wild-type and *Stim1*$^{\Delta EC}$ mice were challenged with LPS (1 μg/ml) for 16 hours. ECs were loaded for 30 minutes with Fluo-4/AM. (**C**) Representative traces from wild-type and *Stim1*$^{\Delta EC}$ ECs. (**D**) Quantification of oscillation frequency. ECs from wild-type and *Stim1*$^{\Delta EC}$ mice were transduced with adenovirus encoding NFATc3-GFP for 36 hours. Following adenoviral transduction, ECs were treated with LPS for 16 hours. (**E**) Representative images showing NFAT nuclear translocation. Scale bar: 20 μm. Arrowheads indicate the nuclear translocated NFAT. (**F**) Quantification of nuclear NFAT-positive cells. (**G**) NFAT-dependent luciferase activity was measured in wild-type and *Stim1* KD ECs 16 hours after LPS (1 μg/ml) treatment. (**H**) Quantification of cytokine protein expression in wild-type and *Stim1*$^{\Delta EC}$ ECs treated with LPS for 16 hours. Data are mean ± SEM. $^{*}P < 0.05$, $^{**}P < 0.01$, $^{***}P < 0.001$.

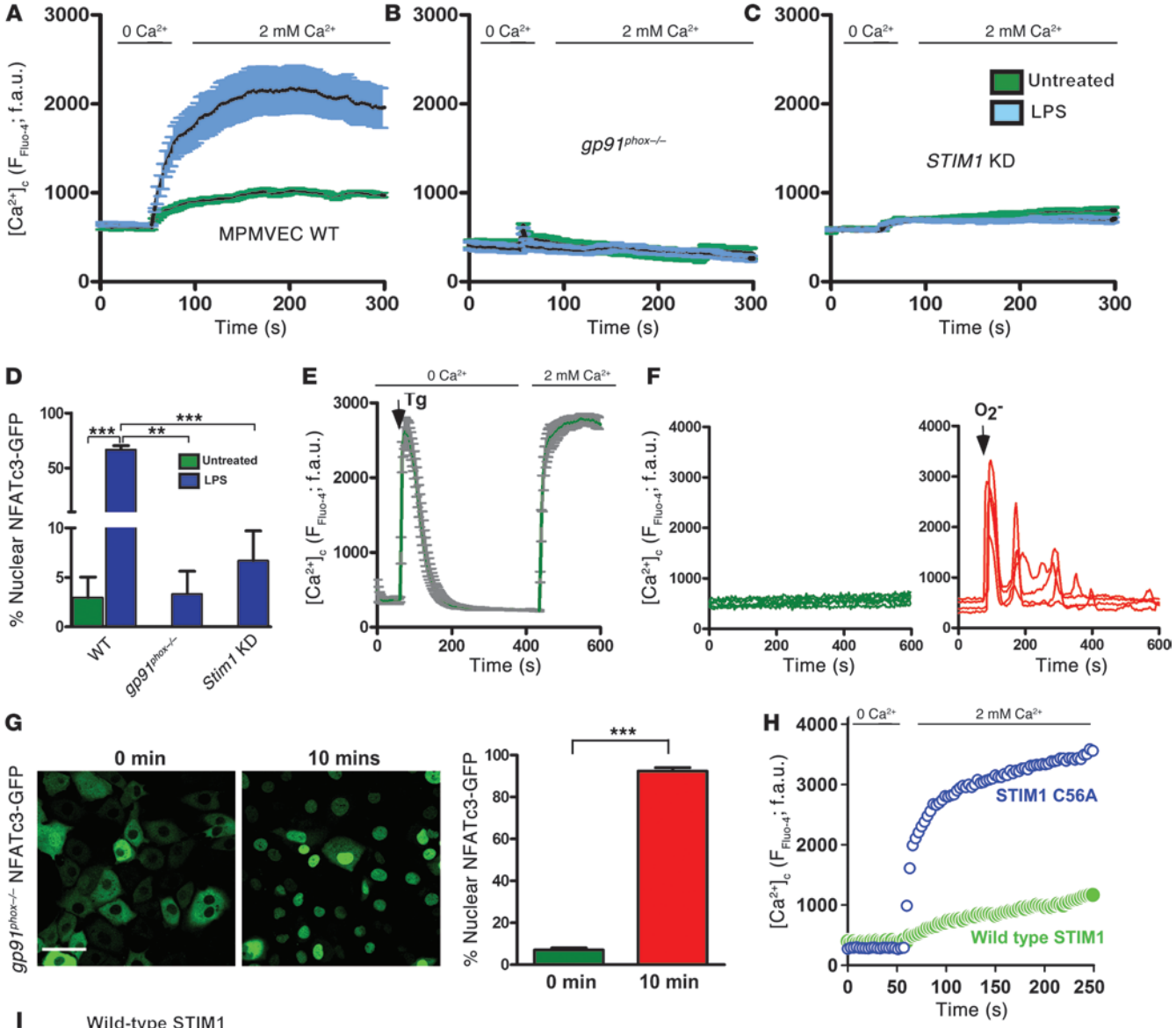

Figure 6

NOX2-derived ROS promotes STIM1-dependent Ca^{2+} entry and NFAT activation after LPS stimulation. Wild-type, *gp91*$^{phox-/-}$, and *Stim1* KD ECs were treated with LPS (1 μg/ml) for 16 hours. (**A**–**C**) Extracellular Ca^{2+} was removed for 5 minutes prior to assessment of SOCe activity in (**A**) wild-type, (**B**) *gp91*$^{phox-/-}$, and (**C**) *Stim1* KD ECs. Wild-type, *gp91*$^{phox-/-}$, and *Stim1* KD ECs were transduced with adenovirus encoding NFATc3-GFP for 36 hours and then treated with LPS (1 μg/ml) for an additional 16 hours. (**D**) Quantification of nuclear NFAT-positive cells. (**E**) *gp91*$^{phox-/-}$ cells loaded with Fluo-4 were treated with thapsigargin (2 μM) under nominally Ca^{2+}-free conditions, followed by addition of 2 mM Ca^{2+} where indicated to assess SOCe. (**F**) Fluo-4–loaded *gp91*$^{phox-/-}$ ECs were treated with (right) or without (left) superoxide (xanthine + xanthine oxidase [$O_2^{\cdot-}$]; 10 nmol/min). (**G**) *gp91*$^{phox-/-}$ ECs were transduced with AdNFATc3-GFP for 36 hours, and nuclear NFATc3-GFP was quantified after $O_2^{\cdot-}$ exposure. Scale bar: 20 μm. (**H**) *gp91*$^{phox-/-}$ ECs were transfected with either STIM1 wild-type or STIM1 C56A mutant constructs. Extracellular Ca^{2+} was removed for 5 minutes prior to the measurement of SOCe activity in Fluo-4–loaded ECs. (**I**) *gp91*$^{phox-/-}$ ECs transiently expressing either wild-type or STIM1 C56A plasmids were transduced with AdNFATc3-GFP for 36 hours, and nuclear NFATc3GFP was quantified. Scale bar: 20 μm. All data are the mean ± SEM of 3 independent experiments, each experiment consisting of triplicate analyses of 20–30 cells. $^{**}P < 0.01$, $^{***}P < 0.001$.

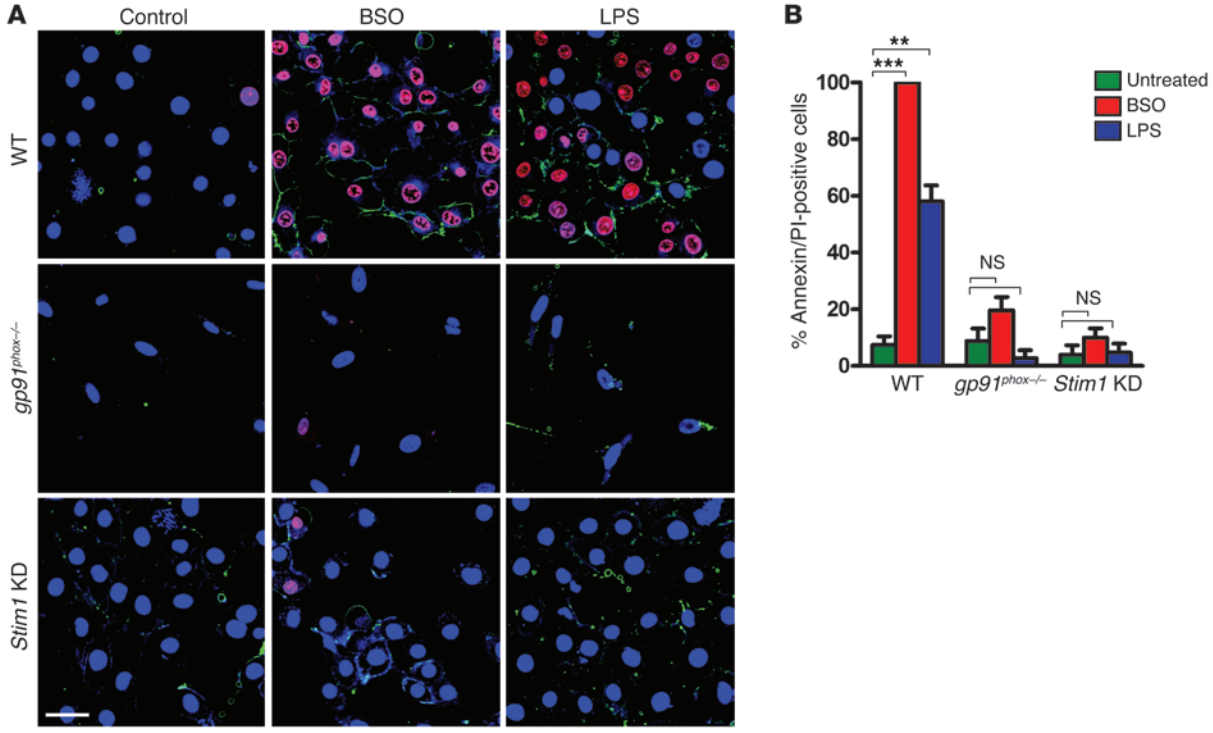

Figure 7
Ablation of STIM1 abrogates LPS-induced EC death. (**A**) Wild-type, *Stim1* KD, and *gp91*$^{phox-/-}$ ECs stimulated with LPS (1 μg/ml) for 48 hours were stained using Annexin V–Alexa Fluor 488 and PI as cell death markers, and Hoechst 33342 was used as a nuclear marker as described in Methods. (**B**) Quantification of dead cells. Scale bar: 20 μm. Data are mean ± SEM. $^{**}P < 0.01$, $^{***}P < 0.001$.

We and others have previously shown that paracrine-derived superoxide triggers Ca^{2+} influx in ECs (16, 36, 37). To examine whether the loss of *gp91*^{phox} impacts endothelial Ca^{2+} entry, we pretreated ECs with thapsigargin and measured Ca^{2+} entry. ECs exhibited robust store-operated Ca^{2+} entry, indicating that loss of *gp91*^{phox} does not account for their failure to trigger LPS-induced Ca^{2+} oscillations, Ca^{2+} entry, and/or NFAT activation (Figure 6E and see Figure 6, B and D). The specificity of the *gp91*^{phox} ablation on NOX2 function was further revealed in experiments showing that paracrine-derived superoxide triggers both Ca^{2+} oscillations (Figure 6F and Supplemental Video 7) and NFAT activation (Figure 6G) in *gp91*$^{phox-/-}$ ECs. Finally, we asked whether ROS-independent activation of STIM1 promotes SOCe and NFAT nuclear accumulation. Ectopic expression of constitutively active STIM1 C56A but not wild-type STIM1 triggered constitutive Ca^{2+} entry (Figure 6H and ref. 14) and NFATc3-GFP nuclear translocation in *gp91*$^{phox-/-}$ ECs (Figure 6I). These results demonstrate that NOX2-dependent STIM1 activation is a crucial step for LPS-induced Ca^{2+} entry and NFAT activation in ECs.

STIM1 signaling contributes to pulmonary vascular EC death. Ca^{2+} is an important second messenger in many cell types, with pleiotropic effects on cell survival. Importantly, in ECs, Ca^{2+} signaling is crucial for the maintenance of barrier function and vascular tone (5). Having demonstrated that *Stim1*$^{\Delta EC}$ mice are protected from inflammatory responses in lung, we speculated that STIM1 may contribute to EC death during inflammatory insults. Therefore, *Stim1* KD ECs were treated with LPS or BSO as a positive control and stained with Annexin V/PI, a marker for cell death. LPS triggered significant cell death in wild-type ECs; however, ECs lacking STIM1 were protected from LPS-induced cell death (Figure 7, A and B). We next questioned whether inhibition of NOX2-derived ROS also prevents LPS-induced cell death. Similar to *Stim1*$^{\Delta EC}$ ECs, ECs lacking *gp91*^{phox} were protected against LPS-induced cell death (Figure 7, A and B). We next extended our in vitro studies to determine whether pulmonary vascular endothelial injury is suppressed by CRAC channel inhibition in the LPS-induced inflammation model. First, we addressed this in an acute setting in which mice were administered LPS (1 mg/kg; i.p.) for 24 hours. We performed immunolabeling of receptor-interacting protein 3 (RIP3), a necrotic cell death marker (38), in lung sections from wild-type and *Stim1*$^{\Delta EC}$ mice. EC-specific STIM1 ablation attenuated the otherwise increased RIP3 expression in VE-Cre and *Stim1*$^{fl/fl}$ control mice, indicating the essential role played by STIM1-mediated Ca^{2+} entry in EC death (Figure 8, A and B). To further examine the role of CRAC channel in EC death, we evaluated the effect of BTP2 in LPS-induced vascular RIP3 expression in vivo. Mice were injected with BTP2 (1 mg/kg i.p.) or vehicle 2 hours after LPS challenge. Lung sections were subjected to immunolabeling for RIP3, and the fluorescence intensity was measured in pulmonary vasculature. Importantly, blockade of Ca^{2+} entry by BTP2 significantly inhibited the vascular RIP3 protein expression resulting from LPS challenge (Figure 8, C and D). Thus, we propose that TLR4/NOX2/STIM1 signaling provides a potential mechanism by which LPS, at least in part, promotes vascular inflammation (Figure 8E).

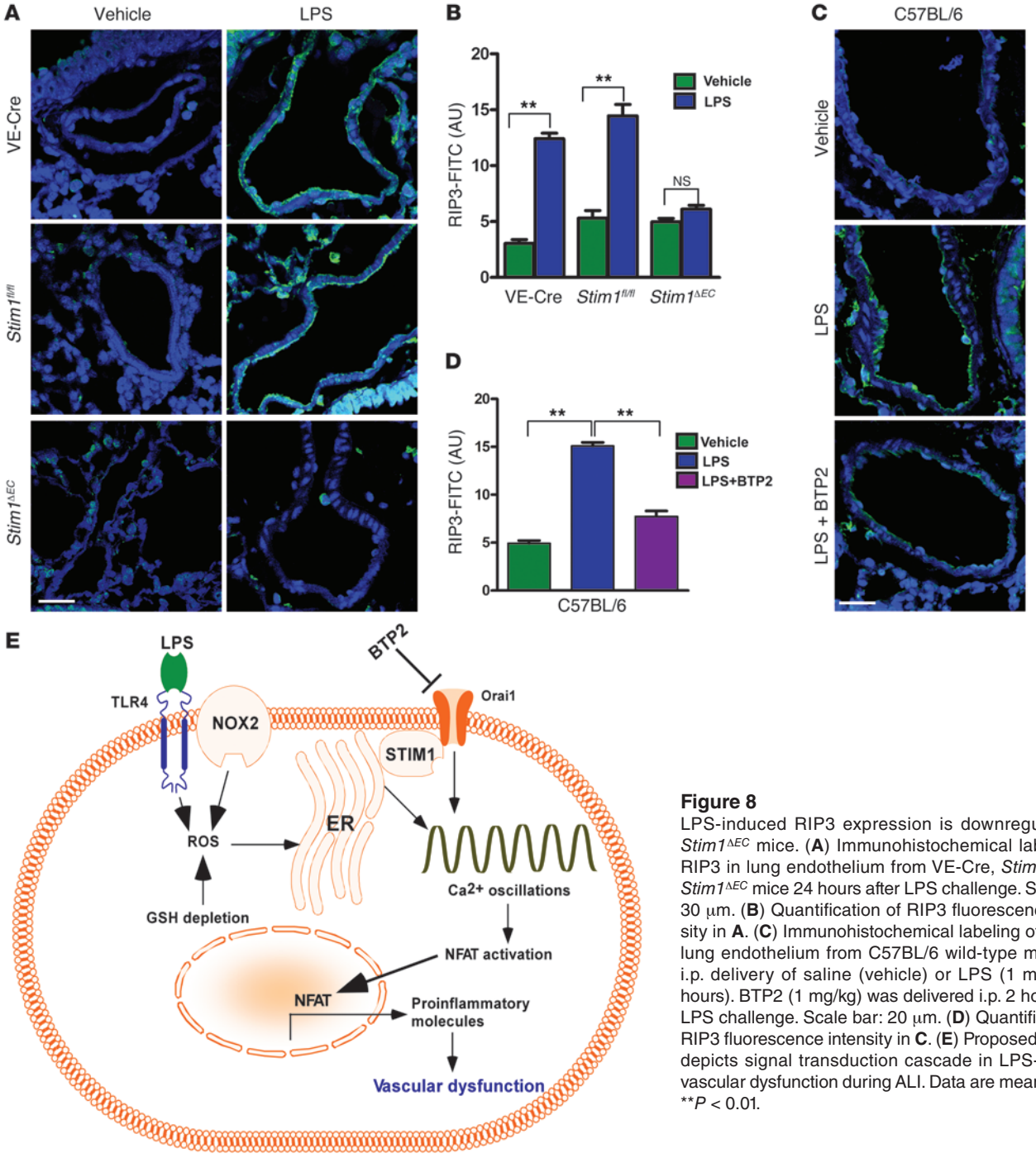

Figure 8
LPS-induced RIP3 expression is downregulated in *Stim1*$^{\Delta EC}$ mice. (**A**) Immunohistochemical labeling of RIP3 in lung endothelium from VE-Cre, *Stim1*$^{fl/fl}$, and *Stim1*$^{\Delta EC}$ mice 24 hours after LPS challenge. Scale bar: 30 μm. (**B**) Quantification of RIP3 fluorescence intensity in **A**. (**C**) Immunohistochemical labeling of RIP3 in lung endothelium from C57BL/6 wild-type mice after i.p. delivery of saline (vehicle) or LPS (1 mg/kg; 24 hours). BTP2 (1 mg/kg) was delivered i.p. 2 hours after LPS challenge. Scale bar: 20 μm. (**D**) Quantification of RIP3 fluorescence intensity in **C**. (**E**) Proposed scheme depicts signal transduction cascade in LPS-induced vascular dysfunction during ALI. Data are mean ± SEM. $^{**}P < 0.01$.

Store-operated Ca^{2+} channel inhibition protects against LPS-induced lung injury. Pulmonary edema resulting from Gram-negative bacterial infection is the first indication of organ failure and the most common cause of sepsis-related death. Recent evidence from in vitro studies and our *Stim1*$^{\Delta EC}$ mouse model data suggest that LPS-induced vascular permeability and lung inflammation are partly driven by a pulmonary endothelial NOX2/STIM1 pathway. To examine the therapeutic potential of this mechanism, we tested the highly effective small-molecule Ca^{2+} channel blocker BTP2 in an animal model of sepsis (39). Wild-type mice were administered LPS (1 mg/kg; i.p.) for 24 hours. Mice were also injected with BTP2 (1 mg/kg i.p.) or vehicle 2 hours after LPS challenge. LPS challenge markedly increased the serum proinflammatory cytokine levels within 6 hours (Figure 9A), followed by leukocyte infiltration at 24 hours, indicating the acute nature of LPS-induced lung injury (Figure 9, B and C). Interestingly, BTP2 administration not only prevented LPS-induced proinflammatory cytokine production (Figure 9A), but also reduced leukocyte infiltration in mouse lung (Figure 9, B and C). BTP2 alone had no effect on either serum cytokine levels or leukocyte infiltration (Figure 9, A–C). These data

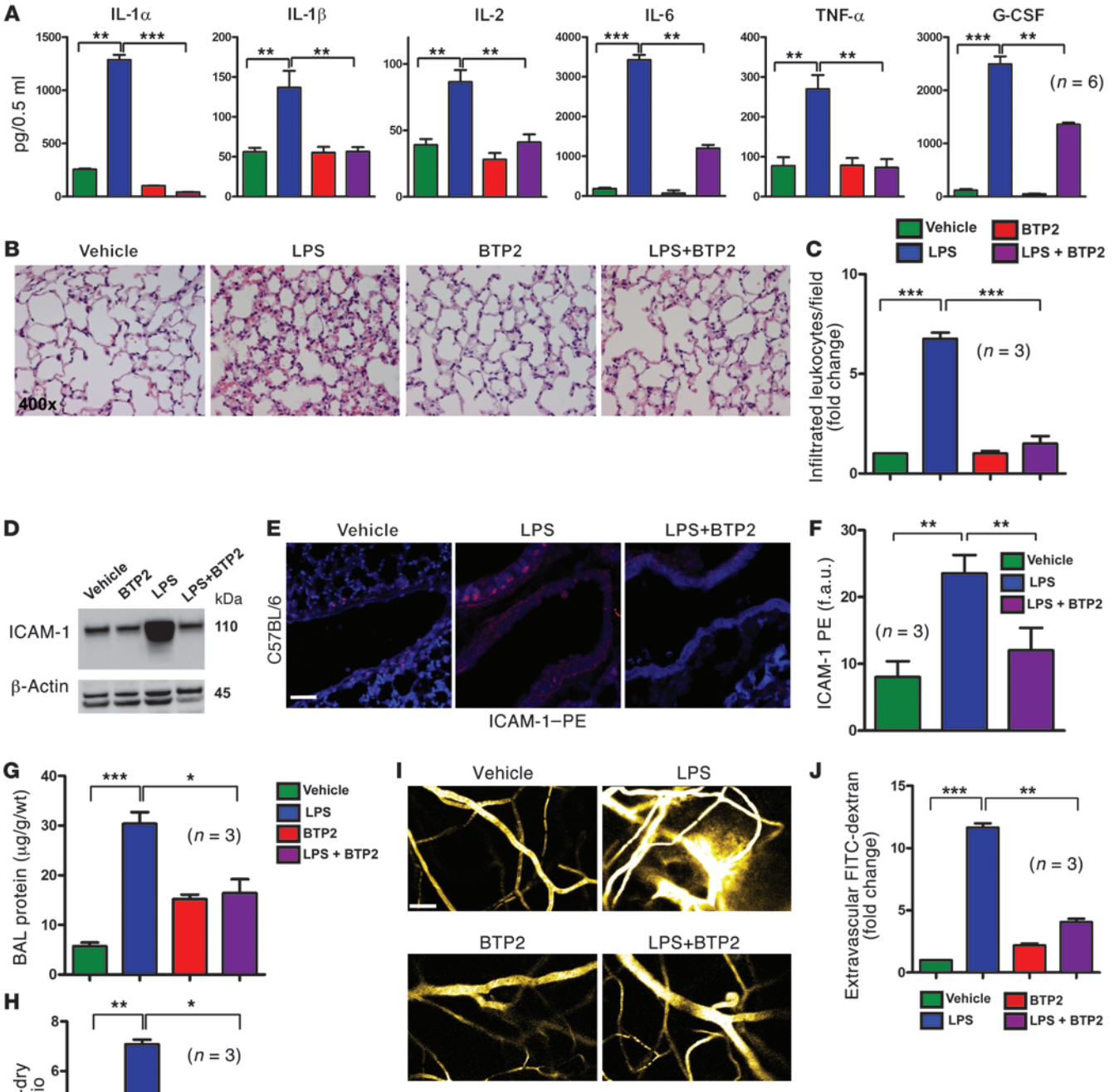

Figure 9

BTP2 attenuates LPS-induced lung inflammation and vascular endothelial integrity loss. C57BL/6 mice were challenged with LPS (1 mg/kg; i.p.), and BTP2 (1 mg/kg; i.p.) was delivered 2 hours after challenge. Saline was used as a vehicle. Samples were collected after 24 hours. (**A**) IL-1α, IL-1β, IL-2, IL-6, TNF-α, and G-CSF were measured in sera from mice. (**B**) Representative photomicrographs of H&E-stained lung sections. Original magnification, ×400. (**C**) Quantification of alveolar leukocytes infiltration. (**D**) Representative Western blot of ICAM-1 induction in ECs treated with LPS and/or BTP2. (**E**) Representative immunohistochemistry images of ICAM-1 using PE in lung sections from treated mice. Scale bar: 20 μm. (**F**) Quantification of ICAM-1 fluorescence intensity. (**G** and **H**) BAL protein content (**G**) and lung weight (**H**) changes are a functional measure of EC activation associated with increased vascular permeability. (**I**) A 0.1- to 0.15-ml bolus of FITC-dextran (70 kDa, 5%w/v) was injected into the animals via facial vein. Anesthetized animals were placed under an intravital 2-photon imaging system, and images were acquired. Vascular permeability was assessed based on fluorescence intensity in the extravascular space around 4–5 regions per mouse. Scale bar: 100 μm. (**J**) Quantification of extravascular FITC-dextran fluorescence. Cumulative data are the mean ± SEM of triplicates and are representative of 3 independent experiments with 3–6 per group as indicated. $^*P < 0.05$, $^{**}P < 0.01$, $^{***}P < 0.001$.

show that 1 mg/kg BTP2 can abolish the systemic cytokine elevation resulting from CRAC channel activation. Vascular ECs sense a wide range of both physiological and pathological signals through various membrane-bound apical surface molecules. ICAM-1 is one such well-characterized molecule and is known to be elevated upon LPS challenge. We next evaluated whether Ca^{2+} entry blockade prevents accumulation of the vascular endothelial inflammatory marker ICAM-1. The increased expression of ICAM-1 protein by LPS exposure was inhibited in ECs treated with 5 μM BTP2 (Figure 9D). Similarly, BTP2 administration in LPS-treated mice led to significant inhibition of ICAM-1 protein expression in arterioles/venules of mice lung sections (Figure 9, E and F). The effect of BTP2 in LPS-induced lung injury reinforces the role of STIM1 in vascular inflammation.

LPS-induced vascular leakage leads to an increase in BAL fluid content (5); however, the role for Ca^{2+} entry in this response has not been established. We next evaluated the effect of SOCe channel blockade on the increased BAL protein accumulation and pulmonary edema resulting from LPS challenge. The increases in both BAL protein content and lung wet/dry ratio was inhibited in mice treated with 1 mg/kg BTP2 (Figure 9, G and H). Notably, BTP2 delivery alone had no effect on mouse lung wet/dry weight ratio but moderately elevated BAL protein levels in vehicle-treated controls (Figure 9 G and H). To evaluate the BTP2 effect on vascular integrity in vivo, we performed live vascular imaging using intravital multiphoton microscopy (see Methods for details). Interestingly, the loss of vascular integrity in LPS-challenged mouse lung as seen both qualitatively (Figure 9I) and quantitatively (Figure 9J) by extravascular FITC-dextran, was abrogated in the BTP2-treated group. Together, these results suggest that SOCe channel blockade is effective in preventing LPS-induced pulmonary vascular permeability and lung edema.

Discussion

Vascular endothelial dysfunction is an established event in acute inflammation (40–42). Upon bacterial insult, both autocrine- and paracrine-derived ROS affect the endothelium, leading to altered gene expression and protein modification, resulting in organ failure (43). We have shown previously that paracrine-derived ROS activates EC Ca^{2+} mobilization (15). However, what remained unclear is how autocrine-derived ROS-triggered Ca^{2+} oscillations could lead to acute inflammation–induced EC dysfunction. The present study investigated the possible effects of inhibiting ROS-induced Ca^{2+} signaling and, further, the effects of limiting Ca^{2+} signaling pathways in EC dysfunction. Importantly, we elucidated the role of STIM1 in EC dysfunction without altering the ROS signaling pathway that participates in microbicidal activity. Using this unique model, we detailed the tightly coupled roles played by NOX2-derived ROS and Ca^{2+} signaling in LPS-induced endothelial activation and the progression to ALI.

LPS is a major component of the bacterial cell wall widely used to induce ALI in murine models (41). LPS-challenged mice show typical pathological evidence of ALI, including increased circulating inflammatory cytokine levels, elevated pulmonary EC activation, higher vascular permeability, and increased alveolar fluid accumulation. ROS overproduction in ECs has been shown to contribute to LPS-induced ALI (44). Although upstream signaling pathways such as the PLC/PKC/PI3K axis are reported to trigger LPS-induced ROS in macrophages (45) and ECs (46), ROS-driven signaling pathways that lead to EC death remain elusive. Our previous investigations showed that ROS production during LPS treatment plays a crucial role in the regulation of Ca^{2+} signaling, which can be prevented by antioxidant supplementation (14). Here, we show that LPS-mediated NOX2-dependent oxidative stress evokes cytosolic Ca^{2+} oscillations in ECs (Figure 5 and Supplemental Figures 2 and 3). Inhibition of NOX2 prevented LPS-induced Ca^{2+} oscillations, supporting our hypothesis that ROS is an essential trigger for LPS-mediated Ca^{2+} oscillations. However, depletion of extracellular Ca^{2+} or blockade of Ca^{2+} channels abrogated Ca^{2+} oscillations without interfering with ROS elevation in ECs. Similarly, depletion of glutathione using BSO to increase ROS gave rise to a sustained pattern of Ca^{2+} oscillations (our unpublished observations). Consistent with this, it has been proposed that cytosolic Ca^{2+} oscillations in ECs are induced by exogenous delivery of oxidants, hypoxia/reoxygenation, or *S*-glutathionylation (16, 47, 48).

LPS-induced ROS in ECs triggers ER Ca^{2+} release via PLC activation (16, 33), which is the initial trigger for Ca^{2+} oscillations. Interestingly, we found that $InsP_3RII$ is uniquely required to maintain LPS-induced Ca^{2+} responses, despite the presence of both $InsP_3RI$ and $InsP_3RIII$ in ECs. This reflects remarkably distinct $InsP_3R$ specificity from classical GPCR agonist-induced Ca^{2+} oscillations which require $InsP_3RI$ (49). These findings indicate that whereas the 3 distinct $InsP_3R$ subtypes may all be capable of mediating Ca^{2+} oscillations, activators selectively engage specific $InsP_3R$ subtypes. In addition to $InsP_3R$ subtype specificity, maintenance of Ca^{2+} oscillations is shown to require SOCe (25, 32). SOCe requires STIM1, the ER luminal Ca^{2+} sensor, which, upon Ca^{2+} store depletion, translocates into ER/plasma membrane junctions and couples to activate Orai1 (50) and possibly transient receptor potential channels (TRPCs) (51, 52). However, we recently revealed that STIM1 can act independently of ER Ca^{2+} as a ROS sensor to induce Ca^{2+} entry (14). Our results using STIM1 C56A mutant constructs showed constitutive Ca^{2+} entry and NFAT activation in *gp91*$^{phox-/-}$ ECs (Figure 6, H and I). Hence, STIM1 can be engaged by ROS during ALI through two distinct mechanisms: $InsP_3$-mediated ER Ca^{2+} depletion and ROS-mediated STIM1 activation.

Agonist-induced Ca^{2+} oscillations influence a multitude of signaling pathways (29, 53). Ca^{2+} oscillations are known to alter inflammatory cytokine expression by differentially activating transcription factors including NFAT and NF-κB (29). The central role of NF-κB in LPS signaling is well established (54, 55). However, our study reveals an alternate inflammatory pathway that requires STIM1-dependent NFAT activity in ECs (Figure 5). Since NFAT mediates TNF-α upregulation, our findings uncover a central role for Ca^{2+} in LPS-induced necrotic cell death. We further demonstrate that RIP3 upregulation is dependent on Ca^{2+} signals that are linked to LPS-induced necroptosis, consistent with previous findings (38).

A major finding in the present study is that post-insult delivery of BTP2 significantly lowers vascular permeability and lung edema. BTP2 is an enticing therapeutic candidate, as it inhibits SOCe without altering baseline intracellular Ca^{2+} levels, suggesting that it does not affect unstimulated cells. Furthermore, mice can tolerate a dosage of up to 30 mg/kg without any systemic toxicity (39). Although BTP2 inhibits the function of CRAC, TRPC3, and TRPC5 channels, while activating TRPM4 channels (56–58), using *Stim1*$^{\Delta EC}$ mice, we reveal STIM1-mediated Ca^{2+} entry as the critical contributor to LPS-induced EC activation and necrotic cell death, the key events in the initiation of ALI. These findings add to a growing list of pathophysiological conditions that are negatively contributed to by STIM-mediated Ca^{2+} entry, including

arterial thrombosis in ischemic brain infraction (59) and hypoxic damage to neurons (60). In contrast, STIM1/Orai1-dependent SOCe is required for T and B cell activation (61), and mutations in STIM1 result in immunodeficiency and autoimmune syndromes (62). Recently, a type 1 diabetic mouse model study reported that downregulation of STIM1 and SERCA3 in coronary ECs enhanced the ER Ca^{2+} leak and store depletion (27). This is in agreement with our work demonstrating a requirement of STIM1 for ER Ca^{2+} homeostasis. Although STIM1 is necessary for endothelium-dependent relaxation, in our model system, STIM1-dependent Ca^{2+} signaling is contributing to vascular inflammation. These distinct and cell type–dependent roles for STIM1 highlight the need for future investigations directed at defining the contributions of STIM1 to other physiological and pathophysiological conditions.

In conclusion, our cellular studies showing ROS-dependent Ca^{2+} mobilization in ECs establish STIM-mediated Ca^{2+} signaling as a crucial event in vascular inflammation during ALI. Future investigations must define the specific STIM-mediated target machinery in order to design effective therapies to alleviate sepsis and ALI. While *Stim1*$^{\Delta EC}$ mice displayed normal baseline characteristics up to 8 weeks, future studies are necessary to understand the role of STIM1 in aging, cardiovascular, and chronic lung diseases. Although Orai channels are the major STIM targets, new information reveals the additional STIM/Orai complex regulators including POST, junctate, SARAF, and CRACR2A (19, 63–66) could also be considered as potential therapeutic targets. Importantly, therapeutic strategies targeting the Ca^{2+} signaling machinery have great advantage over antioxidant-based strategies, since they do not interfere with the microbicidal role of ROS.

Methods

Cell culture. MPMVECs were cultured in DMEM (Invitrogen) supplemented with 10% FBS, GlutaMAX (Invitrogen), 1% antibiotics, and 0.05% EC growth supplement (Upstate). *Stim1* KD MPMVECs were maintained in DMEM with 10% FBS, 1% antibiotics, and 0.05% EC growth supplement GlutaMAX (1%) and puromycin (2 μg/ml, Invitrogen). MPMVECs stably expressing the ROS sensor HyPer-Cyto (Evrogen) were maintained as above but in the presence of G418 (400 μg/ml, Invitrogen). MEFs and an alveolar epithelial carcinoma cell line (A549) were maintained in DMEM supplemented with 10% FBS, 1% GlutaMAX, and 1% antibiotics. Murine macrophage (J774A.1) cell line was maintained in RPMI-1640 medium supplemented with 10% FBS, 1% GlutaMAX, 1% HEPES (Invitrogen), 1% sodium pyruvate (Invitrogen), 1% non-essential amino acids (Invitrogen), and 1% antibiotics.

Lungs from wild-type, *Stim1*$^{\Delta EC}$, *Stim1*$^{fl/fl}$, and VE-Cre mice were harvested, finely minced, and digested in 10 ml collagenase type II (2 mg/ml, Roche). Isolated cells were incubated with anti–PECAM-1 (1:1,000, eBioscience), and ECs bound with antibody were magnetically separated with mouse Anti-Rat Kappa Microbeads (Miltenyi Biotec), according to the manufacturer's instructions.

Generation of stable Stim1 KD ECs. Lentiviruses were generated using 5 lentiviral shRNAs targeting different regions of *Stim1* (MISSION shRNA NM_002467; Sigma-Aldrich) as previously described. ECs transduced with *Stim1*-specific lentiviruses (0.3 MOI) were selected with puromycin (2 μg/ml) for 6 days. After puromycin selection, clones were expanded, and STIM1 protein expression was quantified by immunoblotting using β-actin as loading control.

Measurement of $[Ca^{2+}]_c$ *mobilization*. ECs adherent to 25-mm-diameter glass coverslips were loaded with the cytosolic Ca^{2+} indicator Fluo-4/AM (5 μM, Invitrogen) at room temperature for 30 minutes in extracellular medium (ECM) containing 121 mM NaCl, 5 mM $NaHCO_3$, 10 mM Na-HEPES, 4.7 mM KCl, 1.2 mM KH_2PO_4, 1.2 mM $MgSO_4$, 2 mM $CaCl_2$, 10 mM glucose, and 2.0% BSA, pH 7.4, in the presence of 100 μM sulphinpyrazone and 0.003% pluronic acid. After dye loading, the cells were washed and resuspended in the experimental imaging solution (ECM containing 0.25% BSA) and images recorded every 3 seconds at 488-nm excitation using the Zeiss LSM510 META confocal imaging system with a ×40/1.3 NA oil objective at room temperature. Cytosolic Fluo-4 changes were normalized and presented as F/F_0. To assess Ca^{2+} entry, Ca^{2+} free ECM was used in conjunction with 0.5 mM EGTA; 2 mM Ca^{2+} was added as indicated. Images were analyzed and quantified using ImageJ (NIH) or Zen 2009 (Zeiss) (15).

ROS measurements. MPMVECs stably expressing HyPer-Cyto (67, 68) — a mammalian expression vector encoding a fluorescent sensor, HyPer, that localizes in the cytoplasm and specifically senses submicromolar concentrations of H_2O_2 — were treated with LPS or BSO for 16 hours, and confocal images were obtained with a Zeiss LSM510 using a ×40/1.3 NA oil objective at room temperature and using a 488-nm laser at 2.5% power. Fluorescence was quantified using ImageJ as previously described (68). Alternatively, cells were loaded with H2DCFDA (10 μM) for 30 minutes at 37°C and images obtained as described above.

Immunoblot analysis. Cells were lysed in 1× RIPA lysis buffer (Pierce) supplemented with 0.5 mM DTT and 1× protease inhibitor cocktail (Roche). Protein determination was carried out using the Bradford method. Lysates were then heated at 90°C for 10 minutes and centrifuged briefly for 1 minute. Equivalent amounts of protein were resolved by NuPAGE 4%–12% Bis-Tris Gel (Invitrogen), transferred to nitrocellulose membranes, and immunoblotted using iBlot (Invitrogen). Membranes were probed with primary antibodies anti-STIM1 (44/GOK; BD Biosciences; 1:1,000), anti-gp91^{phox} (53/gp91[phox]; BD Biosciences; 1:1,000), anti-$InsP_3$RIII (2/IP3R-3; BD Biosciences; 1:1,000), anti-$InsP_3$RI (C-20; Santa Cruz Biotechnology Inc.; 1:500) anti-$InsP_3$RII (C-20; Santa Cruz Biotechnology Inc.; 1:500), anti–ICAM-1 (G-5; Santa Cruz Biotechnology Inc.; 1:500), and anti–β-actin (N-21; Santa Cruz Biotechnology Inc.; 1:500); and secondary antibodies goat anti-rabbit and anti-mouse conjugated to horse radish peroxidase (Santa Cruz Biotechnology Inc.; 1:2,000) were used and visualized with enhanced ECL substrate (Amersham).

Annexin V binding and PI staining. To assess the externalization of phosphatidylserine in the plasma membrane as marker for early stage of apoptosis, ECs adherent to 25-mm-diameter glass coverslips were incubated with the conjugate Annexin V–Alexa Fluor 488 (Invitrogen, 1 μg/ml) and propidium iodide (PI; Invitrogen; 0.5 μg/ml) for 15 minutes in Annexin V binding buffer (Invitrogen). Annexin V– and PI-stained cells were visualized by a Zeiss LSM510 confocal imaging system using a ×40 oil objective and later quantified.

AdNFATc3 translocation assay. Recombinant adenovirus encoding NFATc3-GFP was used to evaluate nuclear translocation in cultured cells. Cells were infected with NFATc3-GFP (100 MOI) for 36 hours. Cells were then treated with LPS (1 μg/ml) or BSO (500 μM; Sigma-Aldrich) under different conditions for an additional 16 hours. Confocal monolayer snapshots were obtained with a Zeiss LSM 510 META at ×40/1.3 NA objective, using a 488-nm laser. Cells with nuclear NFATc3-GFP were manually counted in 10 different monolayers and data expressed as percent nuclear translocation under the conditions indicated.

Luciferase assay. 10^6 ECs were transfected with 4 μg of luciferase reporter plasmids with or without binding elements for NFAT in 96-well plates using Mirus LT-1 transfection reagent. After 36 hours, cells were stimulated with LPS (1 μg/ml) for an additional 24 hours. The cells were then lysed using 50 μl of 1× passive lysis buffer (Promega). The luciferase activity was detected using the Bright-Glo Luciferase Assay System (Promega) according to the manufacturer's instructions (Victor ×5 luminometer; PerkinElmer). Values were normalized with appropriate controls.

Generation of Stim1$^{\Delta EC}$ mice and animal experiments. *Stim1$^{\Delta EC}$* mice were generated by breeding male *Stim1$^{fl/fl}$* mice (69) with female B6.Cg-Tg(Cdh5-cre)7Mlia/J;(VE-Cre) mice (stock 006137, The Jackson Laboratory). *Stim1$^{\Delta EC}$* knockout mice were born with no developmental defects and were apparently healthy into adulthood. Germline transmission was confirmed by genotyping of DNA obtained from ear clips. EC-specific knockout of *Stim1* expression was confirmed by protein detection by Western blot analysis in freshly isolated ECs from lung tissues and double staining using anti-CD31 (clone 390; eBiosciences;1:50) and anti-STIM1 (44/GOK; BD Biosciences; 1:100) in aorta sections by immunohistochemistry.

For LPS studies, C57BL/6 wild-type, *Stim1$^{\Delta EC}$*, *Stim1$^{fl/fl}$*, and VE-Cre mice were i.p. administered LPS (*E. coli* O111:B4; Sigma-Aldrich; 1 mg/kg) or vehicle (sterile PBS). Blood samples were collected 6 hours later via the retro-orbital route for ELISA. In experiments using the small-molecule Ca^{2+} entry blocker BTP2 (EMD4Biosciences; 1 mg/kg), an equal volume of vehicle control (DMSO) was administered i.p. 2 hours after LPS administration. Animals were euthanized, and lung tissues were then subjected to histological analysis at 24 hours.

Flow cytometry. Fluorochrome-tagged antibodies CD45 (30-F11) and CD3 (17A2) (eBioscience); rabbit STIM1 antibody (Sigma-Aldrich; catalog S6072); and goat anti-rabbit Alexa Fluor 488 secondary antibodies (Invitrogen) were used for surface and intracellular staining. Spleen lymphocytes from wild-type and *Stim1$^{\Delta EC}$* mice were first stained for surface markers, followed by STIM1 intracellular staining. Aqua LIVE/DEAD Fixable Dead Cell Stain (L34957, Molecular Probes, Invitrogen) was used to gate live cells. Samples were acquired on LSR II analyzers (BD Biosciences) and data analyzed using FlowJo software (Tree Star). Lymphocytes were gated with surface markers and assessed for STIM1 expression.

Endothelial migration assay. Wild-type and *Stim1$^{\Delta EC}$* ECs were seeded at a density of 1.0×10^5 cells/well in 6-well plates overnight to produce a confluent monolayer. A uniform 1.8-mm scratch running the entire length of the well was created using a sterile 200-μl tip. The wells were washed 3 times with PBS to remove the cell debris, and 2 ml fresh complete endothelial growth medium was added. After 24 hours, ECs were washed and fixed with CAMCO Quick Stain II as per the manufacturer's instructions. The wells were photographed at multiple locations using a phase contrast microscope with ×4 objectives. Migration was quantitated using ImageJ software (70), and the results were expressed as percent cell migration (71).

Measurement of inflammatory cytokines. The levels of proinflammatory cytokines 4 hours after systemic administration of LPS were assessed in mouse serum and BAL fluid using a Mouse Inflammatory Cytokines Multi-Analyte ELISArray Kit (SABiosciences) according to the manufacturer's instructions.

Mouse tissue cytokine array. ECs derived from wild-type and *Stim1$^{\Delta EC}$* mice were treated with 1 μg/ml LPS for 16 hours. Tissue cytokine array was performed using the Proteome Profiler Mouse Cytokine Array Kit Panel A (R&D Systems) according to the manufacturer's instructions.

Live lung slice preparation. For ex vivo imaging of lung microvessels, lungs were inflated with 1.5 ml of 2% agarose-HBSS at 37°C, and lungs were stiffened at 4°C as described previously (72). The stiffened lung tissue was placed in EMS-5000 tissue slicer (Electron Microscopy Sciences) and approximately 200-μm slices were used for Ca^{2+} imaging. The slices were then loaded with 15 μM Flou-4 AM and 10 μg/ml AcLDL (endothelial marker) in ECM medium in the presence of 100 μM sulphinpyrazone and 0.2% pluronic acid for 60 minutes at 37°C. Slices were subsequently rinsed in Ca^{2+} imaging buffer before 2-photon imaging.

In vivo FITC-dextran vascular leakage. Mice were anesthetized with ketamine/xylazine (100/10 mg/kg) and then injected with FITC-dextran (70 kDa, 5% w/v in saline; Molecular Probes, Invitrogen) and allowed to rest for 10 minutes. Under prolonged anesthesia, mice were restrained, and vascular microvessels in the ear pinna were imaged using a ×20 water immersion objective in a Zeiss 710 META NLO 2-photon microscope equipped with a Chameleon Coherent IR laser. Images were collected in different regions within the ear pinna and were quantified for extravascular FITC-dextran using ImageJ.

Immunohistochemistry. Tissue sections were deparaffinized by 2 changes of xylene for 5 minutes each; slides were then rehydrated in 2 changes of 100% ethanol for 3 minutes, followed by 95% and 80% ethanol for 1 minute, and rinsed in distilled water. Sections were boiled in sodium citrate buffer (10 mM sodium citrate, 0.05% Tween 20, pH 6.0) for 35 minutes. Slides were allowed to cool and blocked with 1% BSA, 3% donkey serum in PBS for 1 hour. Slides were then incubated with primary anti-CD31 (clone 390; eBiosciences;1:50), anti–ICAM-1 (G-5; Santa Cruz Biotechnology Inc.; 1:500), anti-STIM1 (44/GOK; BD Biosciences; 1:100), or anti-RIP3 (CT; ProSci; 1:50) at 4°C overnight. Slides were washed 3 times with PBS/Tween 20, followed by incubation with diluted secondary fluorescent antibodies (Alexa Flour 594/488; 1:200) for 1 hour. After final washing, slides were mounted with antifade gold containing DAPI (Invitrogen) and imaged using a ×40/1.5 NA oil objective in an LSM510 META confocal imaging system.

BAL protein analysis and lung wet/dry ratios. BAL fluid was obtained from the right lung. BAL fluid was obtained by instilling 3 times 0.5-ml aliquots of saline into the right lung by a 22-gauge Abbocath-T catheter (Abbott). Approximately 800 μl lavage fluid was retrieved per mouse, and samples were centrifuged and supernatants stored at –80°C for subsequent analysis of protein content using the Bradford assay.

For determination of lung wet/dry ratios, the left lung blotted on filter paper was weighed and subsequently dried for 3 days in an oven at 65°C. The ratio of wet weight to dry weight represents tissue edema.

Lung histology. Harvested lungs were fixed in 10% formalin. Tissues were embedded in paraffin. Four-micrometer-thick sections were stained with H&E and analyzed by light microscopy. Infiltrated neutrophil numbers were determined by counting over 10 fields at ×400 magnification.

Genotyping. Genomic DNA from 2- to 4-mm ear clips from mice was isolated using a DNeasy Blood & Tissue Kit (QIAGEN) as per the manufacturer's recommendations. PCR was performed using FailSafe PCR 2× premix H (Epicentre) supplemented with Taq DNA polymerase (GenScript) in accordance to the manufacturers' instructions. The following primer pairs were used to identify specific genomic fragments: CRE transgene o1MR1084 5′-GCGGTCTGGCAGTAAAAACTATC and oIMR1085 5′-GTGAAACAGCATTGCTGTCACTT; internal control oIMR7338 5′-CTAGGCCACAGAATTGAAAGATCT and oIMR7339 5′-GTAGGTGGAAATTCTAGAATCATC. Conditions for amplification were 94°C for 3 minutes, 40 cycles of 30 seconds at 94°C, 60 seconds at 51.7°C, 60 seconds at 72°C, and a final extension at 72°C for 2 minutes.

The following primers were used to identify wild-type and knockout genotypes: MOP413: Stim1 WT 5′-CGATGGTCTCACGGTCTCTAGTTC, MOP215: Stim1 knockout 5′-AACGTCTTGCAGTTGCTGTAGGC, and MOP216: Stim1 AS 5′-GGCTCTGCTGACCTGGAACTATAGTG. Amplification conditions were as follows: 96°C for 3 minutes, 40 cycles of 20 seconds at 96°C, 35 seconds at 60°C, 45 seconds at 72°C, and a final extension at 72°C for 5 minutes in an Eppendorf Mastercycler pro. The PCR products were resolved in 1.2% agarose gel at 75 V for 2 hours and interpreted in a UV transillumination chamber. The presence of the knockout band at 580 bp and flox band at 399 bp and the absence of WT band at 348 bp indicates the knockout genotype of *Stim1*.

Statistics. All statistical comparisons between groups were analyzed using 2-tailed Student's *t* test. Differences in means among multiple data sets were analyzed using 1-way or 2-way ANOVA with the Bonferroni post-test unless otherwise indicated. *P* values less than 0.05 were

considered significant in all analyses. The data were computed using GraphPad Prism version 5.0.

Study approval. All animal experiments were approved by the Temple University IACUC (approval nos. 3303 and 3302).

Acknowledgments

This work was supported by NIH grants HL086699 (to M. Madesh), 1S10RR027327-01 (to M. Madesh), and 1R21HL109920-01 (to M. Madesh and J. Soboloff). We thank Anjana Rao (La Jolla Institute for Allergy and Immunology, La Jolla, California, USA), Suresh Joseph (Thomas Jefferson University, Philadelphia, Pennsylvania, USA), and Gary Koretzky (University of Pennsylvania, Philadelphia, Pennsylvania, USA) for providing the *Stim1*$^{fl/fl}$ mice, $InsP_3RI$ antibody, and NFAT-luciferase plasmid construct, respectively. We are grateful to Aron B. Fisher, G. Scott Worthen, and Troy Stevens for critical comments on the results.

Received for publication July 5, 2012, and accepted in revised form November 30, 2012.

Address correspondence to: Muniswamy Madesh, Center for Translational Medicine, 950 MERB, 3500 N. Broad Street, Temple University, Philadelphia, Pennsylvania 19140, USA. Phone: 215.707.5465; Fax: 215.707.9890; E-mail: madeshm@temple.edu.

1. Russell JA. Management of sepsis. *N Engl J Med*. 2006;355(16):1699–1713.
2. Angus DC, Linde-Zwirble WT, Lidicker J, Clermont G, Carcillo J, Pinsky MR. Epidemiology of severe sepsis in the United States: analysis of incidence, outcome, and associated costs of care. *Crit Care Med*. 2001;29(7):1303–1310.
3. Hotchkiss RS, Karl IE. The pathophysiology and treatment of sepsis. *N Engl J Med*. 2003; 348(2):138–150.
4. Martin GS, Mannino DM, Eaton S, Moss M. The epidemiology of sepsis in the United States from 1979 through 2000. *N Engl J Med*. 2003;348(16):1546–1554.
5. Mehta D, Malik AB. Signaling mechanisms regulating endothelial permeability. *Physiol Rev*. 2006;86(1):279–367.
6. Matthay MA, Folkesson HG, Clerici C. Lung epithelial fluid transport and the resolution of pulmonary edema. *Physiol Rev*. 2002;82(3):569–600.
7. Lee JW, Fang X, Gupta N, Serikov V, Matthay MA. Allogeneic human mesenchymal stem cells for treatment of E. coli endotoxin-induced acute lung injury in the ex vivo perfused human lung. *Proc Natl Acad Sci U S A*. 2009;106(38):16357–16362.
8. Goldblum SE, Brann TW, Ding X, Pugin J, Tobias PS. Lipopolysaccharide (LPS)-binding protein and soluble CD14 function as accessory molecules for LPS-induced changes in endothelial barrier function, in vitro. *J Clin Invest*. 1994;93(2):692–702.
9. Baluk P, et al. TNF-alpha drives remodeling of blood vessels and lymphatics in sustained airway inflammation in mice. *J Clin Invest*. 2009; 119(10):2954–2964.
10. Czermak BJ, et al. Mechanisms of enhanced lung injury during sepsis. *Am J Pathol*. 1999; 154(4):1057–1065.
11. Phillipson M, Kubes P. The neutrophil in vascular inflammation. *Nat Med*. 2011;17(11):1381–1390.
12. Berridge MJ, Bootman MD, Roderick HL. Calcium signalling: dynamics, homeostasis and remodelling. *Nat Rev Mol Cell Biol*. 2003;4(7):517–529.
13. Bogeski I, Kappl R, Kummerow C, Gulaboski R, Hoth M, Niemeyer BA. Redox regulation of calcium ion channels: chemical and physiological aspects. *Cell Calcium*. 2011;50(5):407–423.
14. Hawkins BJ, et al. S-glutathionylation activates STIM1 and alters mitochondrial homeostasis. *J Cell Biol*. 2010;190(3):391–405.
15. Madesh M, et al. Selective role for superoxide in InsP3 receptor-mediated mitochondrial dysfunction and endothelial apoptosis. *J Cell Biol*. 2005;170(7):1079–1090.
16. Hu Q, Zheng G, Zweier JL, Deshpande S, Irani K, Ziegelstein RC. NADPH oxidase activation increases the sensitivity of intracellular Ca2+ stores to inositol 1,4,5-trisphosphate in human endothelial cells. *J Biol Chem*. 2000;275(21):15749–15757.
17. Liou J, et al. STIM is a Ca^{2+} sensor essential for Ca^{2+}-store-depletion-triggered Ca^{2+} influx. *Curr Biol*. 2005;15(13):1235–1241.
18. Roos J, et al. STIM1, an essential and conserved component of store-operated Ca^{2+} channel function. *J Cell Biol*. 2005;169(3):435–445.
19. Soboloff J, Rothberg BS, Madesh M, Gill DL. STIM proteins: dynamic calcium signal transducers. *Nat Rev Mol Cell Biol*. 2012;13(9):549–565.
20. Feske S, et al. A mutation in Orai1 causes immune deficiency by abrogating CRAC channel function. *Nature*. 2006;441(7090):179–185.
21. Vig M, et al. CRACM1 is a plasma membrane protein essential for store-operated Ca^{2+} entry. *Science*. 2006;312(5777):1220–1223.
22. Zhang SL, et al. Genome-wide RNAi screen of Ca(2+) influx identifies genes that regulate Ca(2+) release-activated Ca(2+) channel activity. *Proc Natl Acad Sci U S A*. 2006;103(24):9357–9362.
23. Xiao B, Coste B, Mathur J, Patapoutian A. Temperature-dependent STIM1 activation induces Ca(2)+ influx and modulates gene expression. *Nat Chem Biol*. 2011;7(6):351–358.
24. Mancarella S, et al. Hypoxia-induced acidosis uncouples the STIM-Orai calcium signaling complex. *J Biol Chem*. 2011;286(52):44788–44798.
25. Parekh AB. Decoding cytosolic Ca2+ oscillations. *Trends Biochem Sci*. 2011;36(2):78–87.
26. Muller MR, Rao A. NFAT, immunity and cancer: a transcription factor comes of age. *Nat Rev Immunol*. 2010;10(9):645–656.
27. Estrada IA, et al. STIM1 restores coronary endothelial function in type 1 diabetic mice. *Circ Res*. 2012;111(9):1166–1175.
28. Soboloff J, Madesh M, Gill DL. Sensing cellular stress through STIM proteins. *Nat Chem Biol*. 2011;7(8):488–492.
29. Dolmetsch RE, Xu K, Lewis RS. Calcium oscillations increase the efficiency and specificity of gene expression. *Nature*. 1998;392(6679):933–936.
30. Park HS, Jung HY, Park EY, Kim J, Lee WJ, Bae YS. Cutting edge: direct interaction of TLR4 with NAD(P)H oxidase 4 isozyme is essential for lipopolysaccharide-induced production of reactive oxygen species and activation of NF-kappa B. *J Immunol*. 2004;173(6):3589–3593.
31. Lamb FS, Hook JS, Hilkin BM, Huber JN, Volk AP, Moreland JG. Endotoxin priming of neutrophils requires endocytosis and NADPH oxidase-dependent endosomal reactive oxygen species. *J Biol Chem*. 2012;287(15):12395–12404.
32. Dupont G, Combettes L, Bird GS, Putney JW. Calcium oscillations. *Cold Spring Harb Perspect Biol*. 2011;3(3).
33. Zhang L, et al. Lipopolysaccharide activated phosphatidylcholine-specific phospholipase C and induced IL-8 and MCP-1 production in vascular endothelial cells. *J Cell Physiol*. 2011;226(6):1694–1701.
34. Hawkins BJ, Madesh M, Kirkpatrick CJ, Fisher AB. Superoxide flux in endothelial cells via the chloride channel-3 mediates intracellular signaling. *Mol Biol Cell*. 2007;18(6):2002–2012.
35. Kar P, Nelson C, Parekh AB. Selective activation of the transcription factor NFAT1 by calcium microdomains near Ca2+ release-activated Ca2+ (CRAC) channels. *J Biol Chem*. 2011;286(17):14795–14803.
36. Hawkins BJ, et al. G protein-coupled receptor Ca2+-linked mitochondrial reactive oxygen species are essential for endothelial/leukocyte adherence. *Mol Cell Biol*. 2007;27(21):7582–7593.
37. Hu Q, Yu ZX, Ferrans VJ, Takeda K, Irani K, Ziegelstein RC. Critical role of NADPH oxidase-derived reactive oxygen species in generating Ca2+ oscillations in human aortic endothelial cells stimulated by histamine. *J Biol Chem*. 2002; 277(36):32546–32551.
38. Gunther C, et al. Caspase-8 regulates TNF-alpha-induced epithelial necroptosis and terminal ileitis. *Nature*. 2011;477(7364):335–339.
39. Ohga K, Takezawa R, Arakida Y, Shimizu Y, Ishikawa J. Characterization of YM-58483/BTP2, a novel store-operated Ca2+ entry blocker, on T cell-mediated immune responses in vivo. *Int Immunopharmacol*. 2008;8(13–14):1787–1792.
40. Varani J, Ward PA. Mechanisms of endothelial cell injury in acute inflammation. *Shock*. 1994; 2(5):311–319.
41. Andonegui G, et al. Endothelium-derived toll-like receptor-4 is the key molecule in LPS-induced neutrophil sequestration into lungs. *J Clin Invest*. 2003;111(7):1011–1020.
42. Aird WC. Endothelium as a therapeutic target in sepsis. *Curr Drug Targets*. 2007;8(4):501–507.
43. Wu SQ, Aird WC. Thrombin, TNF-alpha, and LPS exert overlapping but nonidentical effects on gene expression in endothelial cells and vascular smooth muscle cells. *Am J Physiol Heart Circ Physiol*. 2005;289(2):H873–H885.
44. Hsu HY, Wen MH. Lipopolysaccharide-mediated reactive oxygen species and signal transduction in the regulation of interleukin-1 gene expression. *J Biol Chem*. 2002;277(25):22131–22139.
45. Bae YS, et al. Macrophages generate reactive oxygen species in response to minimally oxidized low-density lipoprotein: toll-like receptor 4- and spleen tyrosine kinase-dependent activation of NADPH oxidase 2. *Circ Res*. 2009;104(2):210–218, 221p following 218.
46. Simon F, Fernandez R. Early lipopolysaccharide-induced reactive oxygen species production evokes necrotic cell death in human umbilical vein endothelial cells. *J Hypertens*. 2009;27(6):1202–1216.
47. Lock JT, Sinkins WG, Schilling WP. Effect of protein S-glutathionylation on Ca2+ homeostasis in cultured aortic endothelial cells. *Am J Physiol Heart Circ Physiol*. 2011;300(2):H493–H506.
48. Zhu L, Luo Y, Chen T, Chen F, Wang T, Hu Q. Ca2+ oscillation frequency regulates agonist-stimulated gene expression in vascular endothelial cells. *J Cell Sci*. 2008;121(pt 15):2511–2518.
49. Hattori M, et al. Distinct roles of inositol 1,4,5-trisphosphate receptor types 1 and 3 in Ca2+ signaling. *J Biol Chem*. 2004;279(12):11967–11975.
50. Luik RM, Wang B, Prakriya M, Wu MM, Lewis RS. Oligomerization of STIM1 couples ER calcium depletion to CRAC channel activation. *Nature*. 2008;454(7203):538–542.
51. Cheng KT, Liu X, Ong HL, Swaim W, Ambudkar

IS. Local Ca(2)+ entry via Orai1 regulates plasma membrane recruitment of TRPC1 and controls cytosolic Ca(2)+ signals required for specific cell functions. *PLoS Biol*. 2011;9(3):e1001025.
52. Huang GN, et al. STIM1 carboxyl-terminus activates native SOC, I(crac) and TRPC1 channels. *Nat Cell Biol*. 2006;8(9):1003–1010.
53. Clapham DE. Calcium signaling. *Cell*. 2007; 131(6):1047–1058.
54. Wada Y, et al. Preconditioning of primary human endothelial cells with inflammatory mediators alters the "set point" of the cell. *FASEB J*. 2005;19(13):1914–1916.
55. Tiruppathi C, et al. Role of NF-kappaB-dependent caveolin-1 expression in the mechanism of increased endothelial permeability induced by lipopolysaccharide. *J Biol Chem*. 2008; 283(7):4210–4218.
56. He LP, Hewavitharana T, Soboloff J, Spassova MA, Gill DL. A functional link between store-operated and TRPC channels revealed by the 3,5-bis(trifluoromethyl)pyrazole derivative, BTP2. *J Biol Chem*. 2005;280(12):10997–11006.
57. Takezawa R, et al. A pyrazole derivative potently inhibits lymphocyte Ca2+ influx and cytokine production by facilitating transient receptor potential melastatin 4 channel activity. *Mol Pharmacol*. 2006;69(4):1413–1420.
58. Zitt C, et al. Potent inhibition of Ca^{2+} release-activated Ca^{2+} channels and T-lymphocyte activation by the pyrazole derivative BTP2. *J Biol Chem*. 2004;279(13):12427–12437.
59. Varga-Szabo D, et al. The calcium sensor STIM1 is an essential mediator of arterial thrombosis and ischemic brain infarction. *J Exp Med*. 2008;205(7):1583–1591.
60. Berna-Erro A, et al. STIM2 regulates capacitive Ca2+ entry in neurons and plays a key role in hypoxic neuronal cell death. *Sci Signal*. 2009;2(93):ra67.
61. Matsumoto M, Fujii Y, Baba A, Hikida M, Kurosaki T, Baba Y. The calcium sensors STIM1 and STIM2 control B cell regulatory function through interleukin-10 production. *Immunity*. 2011;34(5):703–714.
62. Picard C, et al. STIM1 mutation associated with a syndrome of immunodeficiency and autoimmunity. *N Engl J Med*. 2009;360(19):1971–1980.
63. Krapivinsky G, Krapivinsky L, Stotz SC, Manasian Y, Clapham DE. POST, partner of stromal interaction molecule 1 (STIM1), targets STIM1 to multiple transporters. *Proc Natl Acad Sci U S A*. 2011;108(48):19234–19239.
64. Srikanth S, Jew M, Kim KD, Yee MK, Abramson J, Gwack Y. Junctate is a Ca2+-sensing structural component of Orai1 and stromal interaction molecule 1 (STIM1). *Proc Natl Acad Sci U S A*. 2012;109(22):8682–8687.
65. Palty R, Raveh A, Kaminsky I, Meller R, Reuveny E. SARAF inactivates the store operated calcium entry machinery to prevent excess calcium refilling. *Cell*. 2012;149(2):425–438.
66. Srikanth S, Jung HJ, Kim KD, Souda P, Whitelegge J, Gwack Y. A novel EF-hand protein, CRACR2A, is a cytosolic Ca2+ sensor that stabilizes CRAC channels in T cells. *Nat Cell Biol*. 2010;12(5):436–446.
67. Belousov VV, et al. Genetically encoded fluorescent indicator for intracellular hydrogen peroxide. *Nat Methods*. 2006;3(4):281–286.
68. Mallilankaraman K, Gandhirajan RK, Hawkins BJ, Madesh M. Visualization of vascular Ca2+ signaling triggered by paracrine derived ROS. *J Vis Exp*. 2011;(58).
69. Oh-Hora M, et al. Dual functions for the endoplasmic reticulum calcium sensors STIM1 and STIM2 in T cell activation and tolerance. *Nat Immunol*. 2008;9(4):432–443.
70. Ridley AJ, et al. Cell migration: integrating signals from front to back. *Science*. 2003; 302(5651):1704–1709.
71. Craige SM, et al. NADPH oxidase 4 promotes endothelial angiogenesis through endothelial nitric oxide synthase activation. *Circulation*. 2011;124(6):731–740.
72. Bergner A, Sanderson MJ. Acetylcholine-induced calcium signaling and contraction of airway smooth muscle cells in lung slices. *J Gen Physiol*. 2002;119(2):187–198.